NTNU

Norwegian University of
Science and Technology

The Effect of Deformation by Torsion and Subsequent Heat Treatment on the Microstructure of AA6082

Andreas Strande Hjorth

Materials Science and Engineering (MTMT)
Submission date: June 2018
Supervisor: Bjørn Holmedal, IMA
Co-supervisor: Ola Jensrud, IMA
Sergej Makhonya, Raufoss Technology AS

Norwegian University of Science and Technology
Department of Materials Science and Engineering

Preface

This Master's thesis is submitted as the final product of *TMT4905 – Materials Technology, Master's Thesis* at the Department of Materials Science and Engineering at the Norwegian University of Science and Technology. The thesis was supervised by Professor Bjørn Holmedal and co-supervised by Professor Ola Jensrud and Sergej Makhonya, Raufoss Technology. Raufoss Technology AS was co-sponsoring this work together with the Department for Materials Science and Engineering.

I would like to thank Sergej Makhonya and Raufoss Technology AS for providing material and valuable input at the early phases of this work. I would also like to thank Pål Christian Skaret and Trygve Lindahl Schanche for technical assistance and introduction to the testing equipment.

I would especially like to thank my supervisor Professor Bjørn Holmedal for competent and knowledgeable supervision. Also, I thank Professor Ola Jensrud for sharing his deep knowledge about the topic.

Finally, I will thank my fellow students for their social support and fruitful discussions throughout the past five years.

Trondheim, June 2018

Andreas Strande Hjorth

Summary

An AA6082-aluminum alloy is used in the production of suspension components for cars at Raufoss Technology AS. The components are manufactured through a process of several forming and heating steps. Through torsion testing with subsequent heat treatment, it has been found that the alloy is susceptible to recrystallization during heat treatment following deformation. A linear relationship between the heat treatment temperature and Zener-Hollomon parameter Z and risk of recrystallization is proposed. This relationship suggests that there is a risk of a recrystallized microstructure after post-deformation heat treatment at temperatures above $T_{heat\ treatment}\ [℃] = 1355 - 30 \times \ln Z$.

The flow properties of the material during hot working conditions were examined by torsion testing. Constitutive relations are suggested based on the recorded experimental stress-strain curves and strain rate and deformation temperature measurements. The activation energy for hot work is estimated to be Q_{hw} = 170 kJ/mol for the alloy. The experimental data are found to deviate from the suggested constitutive relations at low deformation temperatures (T = 350°C and T = 400°C) and shear strain rates below 1 s^{-1}. The constitutive relations are generally found to correlate with the experimental data at higher strain rates and deformation temperatures.

Sammendrag

En AA6082-aluminiumslegering brukes i produksjon av komponenter til hjuloppheng i personbiler hos Raufoss Technology AS. Komponenten produseres gjennom en prosess med flere forme- og oppvarmingssteg. Gjennom torsjonstesting med etterfølgende varmebehandling har det blitt funnet at legeringen risikerer å gjennomgå rekrystallisering under varmebehandling etter deformasjon. Et lineært forhold mellom varmebehandlingstemperaturen og Zener-Hollomon-parameteren Z og risiko for rekrystallisering er foreslått. Dette forholdet antyder at det er risiko for en rekrystallisert mikrostruktur etter varmebehandling etter deformasjons ved temperaturer over $T_{heat\ treatment}$ [℃] $= 1355 - 30 \times \ln Z$.

Materialets flytegenskaper under forhold tilsvarende varmforming ble undersøkt ved torsjonstesting. Konstitutive relasjoner er foreslått basert på de målte eksperimentelle spennings-tøyningsskurveene og tøyningshastighets- og deformasjonstemperaturmålinger. Aktiveringsenergien for varmforming er anslått til Q_{hw} = 170 kJ/mol for legeringen. De eksperimentelle dataene avviker fra de foreslåtte konstitutive relasjonene ved lave deformasjonstemperaturer (T = 350 og T = 400 ° C) og tøyningshastigheter under 1 s^{-1}. De konstitutive relasjonene korrelerer generelt godt med forsøksdataene ved høyere tøyningshastigheter og deformasjonstemperaturer.

Table of contents

1 Introduction

Car designers and manufacturers have for the past 50 years or so focused on making cars lighter and more fuel efficient (Miller et al., 2000). In recent times, this focus has grown in line with the increased environmental awareness. In the strive for better and more lightweight production cars, manufacturers have for years been choosing aluminum as the material of choice for certain car parts. Compared to steel, aluminum has a low density, about one third, which is especially utilized in moving parts. Aluminum also has good energy absorption properties, making it a good choice in crash components ("The Aluminium Automotive Manual," 2002). One of the companies that have specialized in the production of aluminum suspension parts is Raufoss Technology AS, located in Raufoss, Norway.

The final properties of an aluminum component largely depend on the production process, commonly called thermo-mechanical treatment. To get the desired properties, all process steps from casting to aging must be closely monitored and controlled. This is often a complex series of different heating, cooling and forming steps (Reiso, 2004). Additionally, the composition of aluminum alloys varies over a wide range of different alloying elements and amounts. Each alloying element will influence the properties of the alloy differently. This creates a vast number of different alloys with potentially very different properties regarding strength, toughness, formability, corrosion resistance and more. This supports the importance of investigating the effect of different thermos-mechanical treatments

The design, combined with desired properties, of the final component will often determine the forming methods that are used. At Raufoss Technology, a front lower control arm (FLCA) is produced in AA6082 aluminum by forging with a series of pre-forming steps. This thermo-mechanical process is outlined in Figure 1. The first of these pre-forming steps is *Cross Wedge Rolling* (CWR). During this forming step, the cross-section of a dense, cylindrical workpiece is reduced by a varying degree by two rolling tools. A preliminary project showed that the material undergoes large strains and strain rates during this step. From Figure 1 it is evident that the resulting microstructure after the first forming step is one of the determining factors for the final microstructure.

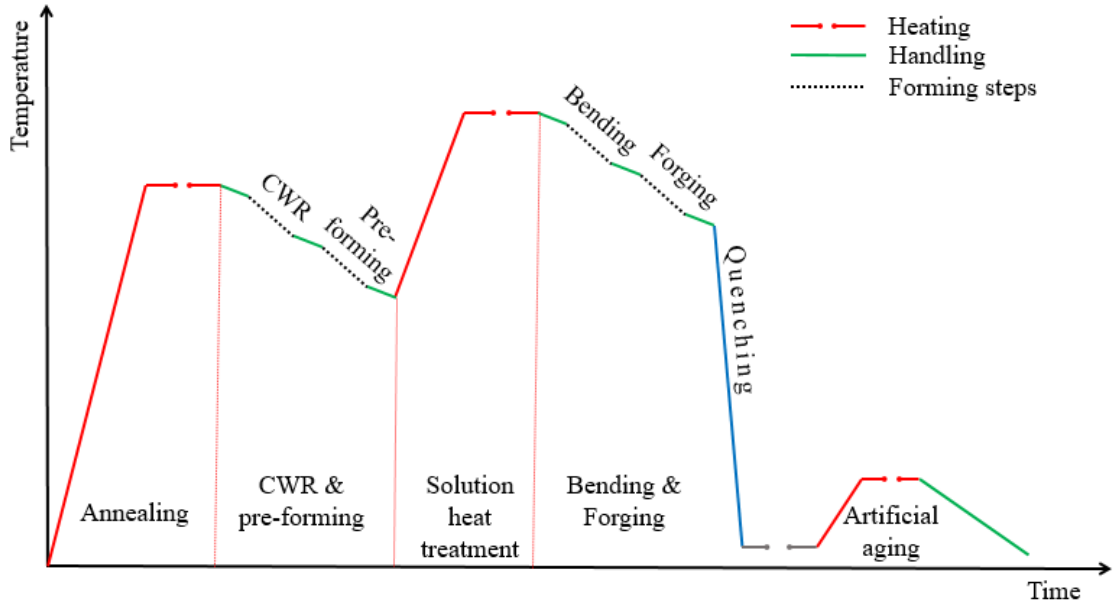

Figure 1 – Thermo-mechanical process for the production of FLCA.

1.1.1 Aims of work

In this thesis, an effort of estimating the effect of a pre-forming step with a subsequent heat treatment is made by torsion testing of the alloy in question. The flow behavior and the dependency upon deformation rate and temperature of the alloy are studied. The microstructure evolution after heat treatment following the pre-forming is also investigated. Relevant theory and terms will be presented and discussed.

2 Theory

To understand the thermo-mechanical treatment and the resulting effects on the material, a theoretical basis for the deformation mechanisms, strengthening mechanisms and microstructural recovery phenomena for the relevant alloy-series is presented. The theory of torsion testing and constitutive relationships at elevated temperatures are also described in this chapter.

2.1 The AlMgSi alloy

AlMgSi alloys, also known as 6xxx-series aluminum alloys, are widely used within the automotive industry. These alloys are generally known to have good strength, high formability, and good fatigue resistance. Depending on the chemical composition, AlMgSi-alloys can also have good corrosion resistance ("The Aluminium Automotive Manual," 2002). The mechanical characteristics of the AlMgSi alloys can be heavily altered and fine-tuned through both thermo-mechanical treatment and addition of other alloying elements. Controlling the process parameters in such processes and the alloy composition are therefore very important for the final properties (Lodgaard, 2000).

The main alloying elements in 6xxx-aluminum are magnesium and silicon. These form Mg_2Si-particles (β-particles) at equilibrium conditions during heat treatment, thus causing these alloys to be heat-treatable. The Mg/Si-ratio for formation of Mg_2Si is 1.73 and the Si and Mg content for most commercial alloys ranges between 0.2–1.5wt% and 0.2–2wt% respectively, with either Si or Mg in excess. Generally, magnesium in excess gives improved corrosion resistance at the expense of strength and formability. Silicon in excess generally gives higher strength but increases the risk of intergranular corrosion (Mondolfo, 1976). The pseudobinary phase diagram for the Al-Mg_2Si system is displayed in Figure 2. According to the diagram, the solubility of Mg_2Si is 1.85wt% at 595˚C (Amado & Daroqui, 2015). The solubility decreases rapidly with decreasing temperature. This causes β-particles to precipitate through a sequence of metastable phases at temperatures below the eutectic temperature. A simplified precipitation sequence for β-particles in an AlMgSi-alloy is generally described in literature as:

$$\text{SSSS} \rightarrow \text{GP zones} \rightarrow \beta'' \rightarrow \beta' \rightarrow \beta\ (Mg_2Si)$$

Here, SSSS is supersaturated solid solution, GP zones are Guinier-Preston zones, and β′ and β″ are metastable phases. The chemical composition, unit cell and morphology of these phases are stated by Vissers et al. (2007) and Marioara, Andersen, Jansen, and Zandbergen (2001),

amongst others. This is described in Table 1. Other intermediary phases in the AlMgSi system are described in literature, e.g. a ribbon-shaped B′($Mg_9Al_3Si_7$), U1(MgAl2Si2) and U2(MgAlSi) (Du et al., 2017; Marioara et al., 2001). These are not relevant for this report and will not be discussed further.

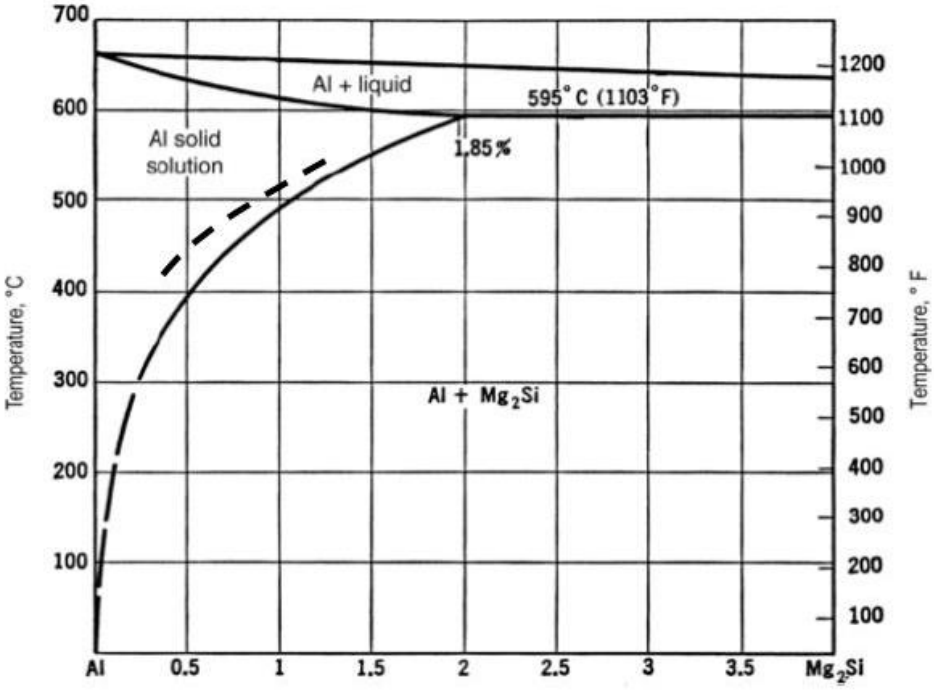

Figure 2 - Al-Mg2Si phase diagram (Amado & Daroqui, 2015)

In addition to magnesium and silicon, industrial 6xxx-aluminum alloys contain several other alloying elements. Iron is often present in a small percentage (< 0.5%) because it is costly to fully remove. Titanium and copper are often added to get increased strength and control grain size. Copper has been found to increase the risk of corrosion, and Larsen (2010) concludes that an AlMgSi alloy containing more than 0.2wt% Cu will be highly susceptible to intergranular corrosion (IGC). Research has found that the presence of copper will influence the composition and morphology of the β-particles. Matsuda, Ikeno, Uetani, and Sato (2001) suggests that copper-containing Q and Q′ particles, where Q′ is a metastable precursor to Q, form alongside or instead of β and β′ particles. Marioara et al. (2007) report several other metastable precursors to Q, namely L, C, QC and QP. Wolverton (2001) suggests that this Q phase has the stoichiometric composition $Al_3Cu_2Mg_9Si_7$. Chromium and manganese act as iron controllers and will combine with iron to form α-Al(Fe,Mn,Cr)Si when present. Ryen, Holmedal, Marthinsen, and Furu (2015) found through TEM studies that small dispersoids with a mean radius of 80 nm forms during homogenization of an AA6082-alloy containing 0.54wt% Mn. Xu, Nagaumi, Han, Zhang, and Zhai (2016) investigate the effect of Mn and Cr on the

deformation behavior and microstructure of an AlMgSiCu-alloy. They conclude that Mn- and Cr-containing α-Al(Fe,Mn,Cr)Si-particles formed during homogenization will hinder the movement of dislocations and grain boundaries during deformation.

Table 1 - Intermediary phases in AlMgSi-alloys.

Phase	Composition	Unit Cell	Morphology	Coherency
GP	$Mg_xAl_{5-x}Si_6$	Primarily monoclinic	Nanometer scale spherical particles or needles of length ~20 nm	Fully coherent with the Al matrix.
β″	Mg_5Si_6	Monoclinic	Needles of length ~50 nm	Fully coherent with the Al matrix in along the b-axis of the unit cell. Semi-coherent along the a and c axis.
β′	$Mg_{1.8}Si$	Hexagonal	Rods of > 100 nm with diameter ~10 nm	Fully coherent with the $\langle 0\ 0\ 1 \rangle_{Al}$ along the c-axis of the unit cell.
β	Mg_2Si	FCC (CaF)	Micron scale plates or cubes	Incoherent

2.2 Strengthening effects in aluminum

The strength of aluminum alloys can be attributed to several factors. The most prevalent strengthening mechanisms in hardenable aluminum alloys will be described in this section.

2.2.1 Dislocation movement in pure aluminum

The deformation of metals occurs through movement of line defects, dislocations, in glide planes in the atomic structure. For a face centered cubic (FCC) structure, like aluminum, there are 12 glide systems located in the close-packed 111}<110> - planes/directions. Dislocation movement can be roughly separated into two categories: Conservative and non-conservative dislocation movement. Conservative dislocation movement refers to the movement of dislocation in a given slip plane. Non-conservative dislocation movement involves dislocation movement across two or more slip planes. The two mechanisms are commonly referenced as

dislocation glide and dislocation climb respectively. The latter requires diffusions of vacancies, which is heavily dependent on thermal energy. The thermal activation of dislocation climb is only reached at elevated temperatures, while dislocation glide will readily occur at room temperature.

2.2.2 Strain hardening

Dislocations in a matrix will be surrounded by a stress field due to the elastic stresses caused by the dislocation. These stress fields interact with the stress field of both other dislocations and solute atoms, either alloying atoms or impurities in solid solution, giving resistance to dislocation movement. Introducing more dislocations through plastic deformation will increase the density of these stress fields, hence increasing the resistance to dislocation movement. Also, dislocations also intersect other dislocations creating *jogs* and *kinks*. The creation of *jogs* can give additional resistance to dislocation movement.

A proportional relationship between the yield stress σ_0 and the square root of the dislocation density $\sqrt{\rho}$ is given by Equation (1 (Dieter, 1988, p. 232). In the referenced equation, σ_i is the resistance to dislocation movement of the crystal lattice, α a constant of value ~ 0.3 – 0.5, G the shear modulus and b the burgers vector.

$$\sigma_0 = \sigma_i + \alpha G b \sqrt{\rho} \qquad (1)$$

2.2.3 Grain boundary strengthening

Grain boundaries act as obstacles for dislocation movement. Hence, the more grain boundaries a dislocation must overcome per length, the greater the resistance to dislocation movement. The Hall-Petch equation describes the relationship between yield stress σ_0 and grain size D:

$$\sigma_0 = \sigma_i + kD^{-1/2} \qquad (2)$$

Here σ_i is the resistance to dislocation movement of the crystal lattice and k is a parameter related to the relative hardening contribution of the grain boundaries. From Equation 2 it is seen that this contribution will be small for large grain sizes and/or low k values. Lohne and Naess (1980) argue that this is the case for aluminum. Also, experimental results deviate from the relation for ultrafine-grained materials. For an Al-Mg-Si alloy, deviation occurred for grains sizes below ~500 nm (Loucif et al., 2012).

Grain boundaries are in general separated into two categories by the degree of crystallographic misorientation between the two adjacent grains. When the angle of misorientation, often indicated by θ, is high, the boundary is termed a high-angle grain boundary (HAGB). When the misalignment is less, θ typically below 10˚ - 15˚, the boundary is termed a low-angle grain boundaries (LAGB). The HABGs have significantly higher surface energy than LABGs. HAGBs are in general associated with the boundary between grains, while LAGBs are associated with the boundary between subgrains.

2.2.4 Hardening from precipitates and dispersoids

Precipitates and dispersoids in solids arise from the nucleation and growth of intermetallic particles within the matrix. These particles can have large influence on both the strength and microstructure of the metal. It is common to categorize particles present in a metal matrix after the structure of the interface between the atomic structure in the matrix and atomic structure in the particle nucleus. The three types of particles commonly described in the literature are *Coherent particles*, *Semi-Coherent particles* and *Incoherent particles*. The characteristics of each type of particle are briefly described below (Lodgaard, 2000):

Coherent particle:	The atomic structure and distances of the matrix and the particle are the same (Figure 3a).
Semi-coherent particle:	The atomic structure and distances of the matrix and the particle have a relationship (Figure 3b).
Incoherent particle:	The atomic configurations are very different (Figure 3c).

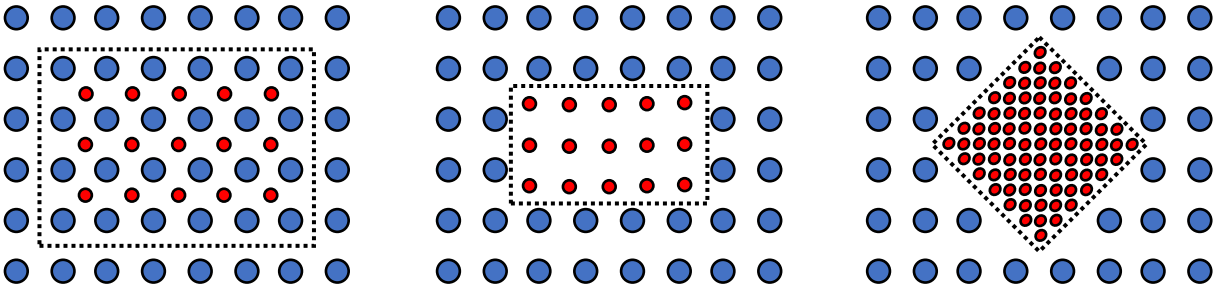

Figure 3 – (a) Coherent particle, (b) - Semi-coherent particle and (c) – Incoherent particle

The coherency and size of the particles formed in the matrix determine how the particle interfere with the movement of dislocations within the material. This interference tends to give resistance to the dislocation movement. This followingly cause hardening effects in the metal, so-called

precipitation hardening. Such effects can come from at least three sources: Coherency strain hardening, Chemical hardening and dispersion hardening (Smallman & Ngan, 2014).

2.2.4.1 Coherency strain hardening

A coherent particle with a matrix mismatch creates a stress field in the surrounding matrix. This act as an obstacle for gliding dislocations, hence increasing the resistance for dislocation movement close to the particle. Dieter (1988, p. 216) presents an estimate of the strengthening contribution where the increase in yield stress $\Delta\sigma$ is proportional to the volume fraction f of coherent particles:

$$\Delta\sigma \approx 2G\varepsilon f \qquad (3)$$

Here ε is a measure of the strain field around each particle. Other, more sophisticated estimates are given, taking into account the particle radius and the burgers vector of the dislocation. These should be evaluated when calculations are necessary.

2.2.4.2 Chemical hardening

Chemical hardening comes from the resistance of shearable coherent or semi-coherent particles to be cut by dislocations. This movement of a dislocation through a particle is illustrated in Figure 4. For this to happen, the particle is required to have a structure allowing dislocation movement, i.e. that the particle is deformable. According to Smallman and Ngan (2014), there are three mechanisms that contribute to chemical hardening: (i) the creation of an additional interface between the particle and the matrix, (ii) the creation of an anti-phase boundary within the particle and (iii) the change in width of a dissociated dislocation passing through a particle with different stacking fault energy than the matrix.

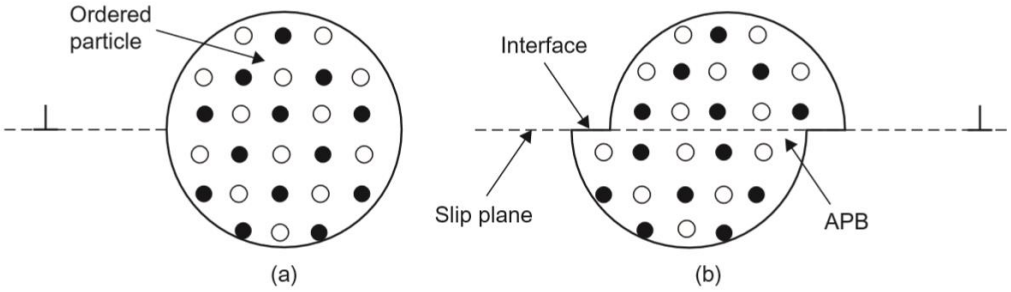

Figure 4 – Cutting of a ordered particle to create a new interface and anti-phase boundary (APB). (Smallman & Ngan, 2014, p. 512)

2.2.4.3 Dispersion hardening

Dispersion hardening generally comes from particles that do not deform with the surrounding matrix, so-called non-deformable particles. These particles will not be cut by passing dislocations and will give rise to dislocation loops around the particle, also called Orowan loops. The formation of such loops is illustrated in Figure 5 (Smallman & Ngan, 2014, p. 511). A moving dislocation line approaching two non-deformable particles will bend around the particles and create dislocation loops around each particle. This causes the dislocation density in the area to increase. The dislocation is free to continue onwards after the interaction. The stress necessary to force the dislocation between two particles separated by distance L in a matrix is given by Equation 4 (Smallman & Ngan, 2014, p. 512)

$$\tau = \alpha G b / L \tag{4}$$

where α is a numerical constant, G is the shear modulus and b is burgers vector. Each passing dislocation will add additional loops around the particle. This creates incremental increases in the necessary stress, giving a rapid strain-hardening effect (Dieter, 1988).

Zhao, Holmedal, and Li (2013) describes the stress contribution of fine dispersoids to the flow stress as

$$\sigma_{\mathrm{Oro}} = 0.81 \frac{MAGb}{2\pi\lambda} \ln \frac{\pi d}{4b} \tag{5}$$

where σ_{Oro} is the Orowan stress, M is the Taylor factor (~ 3), λ is the dispersoid spacing that is a function of the dispersoid diameter d and volume fraction f_V.

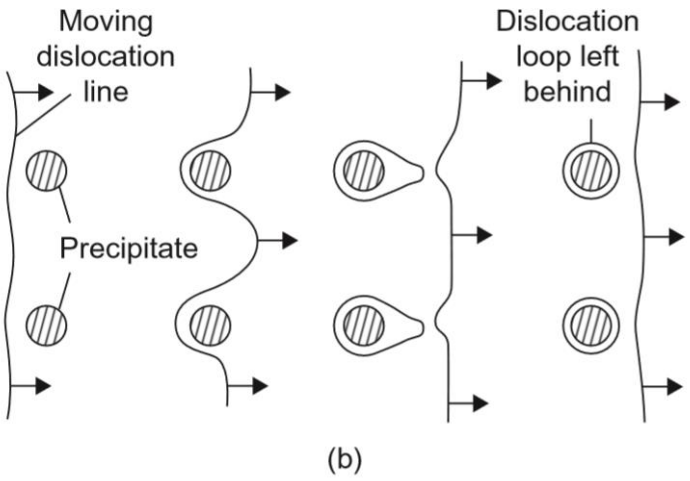

Figure 5 - Interaction between non-shearable particles and moving dislocation. (Smallman & Ngan, 2014, p. 511)

2.3 Recovery, recrystallization and grain growth

During plastic deformation of a material, elastic strain/stress energy is introduced to the matrix through introduction of new dislocations and interfaces. An increase in the number of dislocations in the material is synonymous with an increase in the dislocation density. This causes the elastic energy of the matrix to increase. A practical implication of this effect is that the flow stress of the metal increases. To counteract this increase in elastic energy, metals often undergo one or more of the following processes: (i) recovery, (ii) recrystallization and (iii) grain growth. It is common to separate changes happening during deformation and after deformation. When these processes take place during heating after deformation, so-called annealing, it is termed static annealing phenomena. Recovery and recrystallization taking place during deformation at elevated temperatures are termed dynamic recovery and recrystallization. These two mechanisms can together be called dynamic softening. Recovery, recrystallization and grain growth will be introduced and briefly described in this section based on the work of Humphreys and Hatherly (2004).

2.3.1 Recovery

The process of recovery describes the reduction of strain energy through the formation of cells or subgrains through dislocation movement. After deformation, the dislocations will be tangled in a chaotic manner within a grain. To lower the stored energy, the dislocations go through

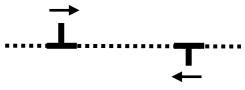

Figure 6 - Annihilation by dislocation glide

annihilations and rearrangements into lower energy configurations. Annihilation can occur when two dislocations of opposite sign (opposite burger vectors) in the same glide plane approach each other, as illustrated in Figure 6. Annihilation may also occur between two dislocations in different glide planes through climb or cross glide. This will reduce the number of dislocations, and hence decrease the dislocation density. Climb requires thermal activation, hence annihilations between glide planes will only occur at higher temperatures. For pure screw dislocations, annihilation can happen through cross-slip.

To further decrease the energy, the remaining dislocations tend to rearrange into lower energy configurations. Metals with high stacking fault energy usually form cells separated by dense dislocation tangles during deformation. When these are annealed, the dislocation tangles tend to form low angle grain boundaries which divide the grain into multiple subgrains. Under certain conditions, the dynamic recovery may cause a subgrain structure to be developed during deformation. Further static recovery after deformation may then lead to subgrain coarsening. Factors that promote a subgrain structure during deformation are high deformation temperature, large strains, low solute content and high stacking fault of the material.

During hot forming of aluminum, thermally activated dislocation climb and cross slip occur more easily. Given a sufficiently high deformation temperature, storage of dislocations and recovery will take place simultaneously at comparable magnitude. The temperature modified strain rate, first described by Zener and Hollomon (1944), will give a representation of the amount of stored deformation energy at a given deformation temperature T [K]. The equation of the parameter now known as the *Zener-Hollomon parameter Z* is shown in Equation 6 (Humphreys & Hatherly, 2004, p. 417).

$$Z = \dot{\varepsilon} \exp\left(\frac{Q}{RT}\right) \qquad (6)$$

In this equation, Q represents the activation energy, R the gas constant and $\dot{\varepsilon}$ the strain rate. For hot deformation, i.e. dynamic recovery, Humphreys and Hatherly (2004, p. 423) gives a relationship between the Zener-Hollomon parameter and the subgrain size D first presented by Furu, Marthinsen, and Nes (1992). This relationship is given in Equation 7.

$$D = K_1 - K_2 \log \mathrm{Z} \qquad (7)$$

K_1 and K_2 are constants.

2.3.2 Recrystallization

Unlike recovery, where the deformed grains remain in their original shape, recrystallization is the nucleation and growth of new, undeformed grains with a low dislocation density. In general, recrystallization depends on a multitude of factors. For a single-phase metal, the amount of strain, mode of deformation, the original microstructure and annealing conditions are factors that determine the static recrystallization behavior. Dynamic recrystallization is determined by the strain rate and deformation temperature. This relation is often represented by the Z-value given in Equation 6. For a metal containing intermetallic particles, like many aluminum alloys, these particles will be an additional factor.

Recrystallized grains will initiate at inhomogeneities in a deformed material. Inhomogeneities commonly found in a deformed alloy are grain boundaries, second phase particles and deformation induced inhomogeneities like shear bands and transition bands. Shear bands are narrow regions with elevated shear stress that run across the grain structure. The driving pressure of recrystallization P_D is equal to the stored deformation energy E_D given by Equation 8.

$$P_D = E_D = \alpha \rho \mathrm{G} b^2 \qquad (8)$$

Here, ρ is the dislocation density, G the shear modulus, b burgers vector and α a constant of the magnitude ~ 0.5. The retarding pressure due to boundary curvature $\mathrm{P_C}$ associated with the growth of a spherical grain of radius R with a HAGB with specific energy γ_b is given in Equation 9.

$$P_C = \frac{2\gamma_b}{R} \qquad (9)$$

In a single-phase alloy matrix, a mechanism called *strain induced boundary migration* (SIBM) is known to explain the initiation of recrystallized grains at grain boundaries. Bulging can occur at the boundary between two grains with different stored energy. The simplest form of SIBM is the expansion of a single subgrain. For these subgrains to grow, the radius R must exceed a critical radius R_{crit} given by Equation 10. P is the driving pressure on the grain boundary and γ_b is the specific boundary energy.

$$R_{\mathrm{crit}} = \frac{4\gamma_b}{P} \qquad (10)$$

2.3.2.1 Effect of second phase particles

Second phase particles will have two major effects on the recrystallization behavior of the metal. How they influence the process are mainly dependent on the particle size. In general, larger particles tend to promote recrystallization through *particle stimulated nucleation of recrystallization* (PSN). Small, finely dispersed particles tend to increase recrystallization resistance through *Zener drag*. The pinning pressure P_Z from a volume fraction f of randomly distributed particles with radius r on a grain boundary with energy γ_b is given by Equation 11.

$$P_Z = \frac{3f\gamma_b}{2r} \tag{11}$$

This relation is valid if the grain diameter (grain size) is much larger than the particle spacing. Applying the pinning pressure from Equation 11, the critical subgrain radius becomes

$$R_{crit} = \frac{4\gamma_b}{P_D - P_Z} \tag{12}$$

P_D now represents the driving pressure on the boundary, i.e. the stored energy from deformation. This equation is a highly simplified representation of an actual recrystallization process. Nevertheless, it highlights the effect of small secondary particles in the matrix.

2.3.2.2 Particle stimulated nucleation of recrystallization (PSN)

Larger particles are associated with a surrounding deformed zone after plastic deformation. These zones will in some cases act as nucleation sites for recrystallization. This requires the misorientation created between the deformed zone and the surrounding matrix during deformation to be great enough to form a HAGB. In general, larger particles and larger deformations will promote particle stimulated nucleation. The initiation of potential nuclei occurs through the growth of a subgrain into the deformed zone as illustrated in Figure 7.

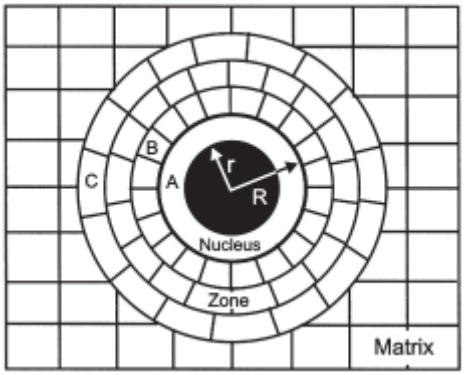

Figure 7 - Growth of nucleus inside the deformed zone (Humphreys & Hatherly, 2004, p. 296)

Once the growth of one subgrain becomes dominant, the further growth is controlled by two opposing pressures given in Equation 8 and 9. The nuclei will continue growing if $P_D > P_C$. From this, a critical particle diameter d_g for the nucleation of a grain that is able to grow into the surrounding matrix is deduced. This diameter is given by Equation 13.

$$d_g = \frac{4\gamma_b}{E_D} = \frac{4\gamma_b}{\alpha\rho G b^2} \qquad (13)$$

For the case of PSN after hot deformation, the Zener-Hollomon parameter Z is introduced as a parameter in Equation 13. The Z-value can then give an estimate of if PSN will occur for a given particle size.

2.3.2.3 Dynamic recrystallization

Dynamic recrystallization is of great concern when a metal is deformed at elevated temperatures. Similar to static recrystallization, the stored deformation energy related to the dislocation density is the driving force for dynamic recrystallization. In Humphreys and Hatherly (2004), it is stated that the function of the dislocation density of the unrecrystallized matrix ρ_m and strain rate $\dot{\varepsilon}$ must exceed a critical value to enable recrystallization. This function is given as $\rho_m^3/\dot{\varepsilon}$. In aluminum, dynamic recovery occurs readily. This will keep the dislocation density of the matrix at a low level, hence counteracting dynamic recrystallization. Dynamic recovery is therefore in general regarded as the dominant dynamic restoration mechanism in aluminum.

Previous research has discovered that structures containing large fractions of high-angle grain boundaries can form during deformation of aluminum without nucleation of new grains. McQueen, Knustad, Ryum, and Solberg (1985) were some of the first to report this result. More

recent research has found similar results (Kassner & Barrabes, 2005; Kassner, Myshlyaev, & McQueen, 1989; Pettersen, Holmedal, & Nes, 2003). This mechanism has been termed *Geometric Dynamic Recrystallization*. It is seen that at large strains, the grains become elongated and the grain boundaries serrated. Because the subgrain size is largely independent of strain during hot deformation, the size of the boundary serrations will approach the size of the subgrains with increasing strain. Eventually, a recrystallized grain will form from the original subgrain and serrated grain boundary. For a given original grain size D_0 and subgrain size D, this will occur at a critical compressive strain given in Equation 14 (Humphreys & Hatherly, 2004, p. 463).

$$\varepsilon_{cr} = \ln\left(\frac{K_1 D_0}{D}\right) = \ln\left(Z^{1/m} D_0\right) + K_3 \qquad (14)$$

Z is the Zener-Hollomon parameter and m, K_1 and K_3 are constants. This equation shows that there is a direct relationship between the original grains size, subgrain size and strain related to the occurrence of *geometric dynamic recrystallization.*

Another form of dynamic recrystallization that is reported to occur in aluminum is *dynamic recrystallization by progressive lattice rotation* (Humphreys & Hatherly, 2004, p. 438). The mechanism behind this phenomenon is not fully understood, but it is stated to be strain-induced and arises from a solute drag (in Al-Mg alloys). It is proposed that grain boundary serrations lead to local lattice rotations when sheared, which give rise to new HAGBs. This phenomenon is said to commonly form a *neckless* of recrystallized grains around pre-existing grains, but that a complete structure of such grains also may occur.

2.3.3 Grain Growth

After primary recrystallization, the recrystallized grains may continue to grow in order to further reduce the energy stored in the material. Some of the remaining stored energy is associated with the grain boundaries. Reducing the total boundary area by increasing grain size will hence lower the stored energy. Since grain growth is dependent on the migration of HAGBs, the mobility of these grain boundaries will be very influential for the grain growth. As discussed earlier, higher temperatures tend to increase the mobility, while solutes and particles tend to pin the boundaries and hinder the movement.

Grain growth can generally be classified by one of two types, *abnormal grain growth*, also known as *secondary recrystallization*, and *normal grain growth*. The latter is a continuous process where the grains coarsens uniformly and reaches a quasi-stationary state where the size distribution of the grains is relatively narrow. Abnormal grain growth is a discontinuous process where a few grains consume smaller grains as they grow. This may result in a microstructure with a few very large grains mixed with smaller grains that may or may not have undergone normal grain growth. Abnormal grain growth has often been reported in severely deformed Al-Mg-Si alloys that have been annealed or solution heat treated after deformation (Park & Lee, 2001; Wang et al., 2015; Yan et al., 2017).

2.3.4 Effect of recrystallization

Recrystallization and grain growth is a concern when doing hot forming on aluminum for different reasons. Sandvik, Jensrud, Gulbrandsen-Dahl, Hallem, and Moe (2010) suggests that a recrystallized structure has inferior fatigue life compared to a fibrous structure. Recrystallization in forged aluminum parts is generally a transition from a fibrous extruded microstructure to an *equiaxed* microstructure. Loss of static strength and ductility, increased risk of intercrystalline corrosion and poorer surface appearance are also mentioned when comparing a recrystallized structure and a fibrous structure in aluminum.

2.4 Torsion test

Torsion tests are often used to investigate flow properties of metals at conditions similar to industrial hot-working conditions, typically temperatures above 0.6 times the melting temperature and strain rates up to 10^3 s^{-1}. The torsion test is a mechanical test method that introduces pure shear stresses and strains to the test specimen. This chapter introduces the theoretical basis for the torsion test as described in the literature.

A bar or tube specimen are twisted with a given moment M_T, commonly measured as *torque* [Nm], that is resisted by an internal resisting moment in the material. The resisting moment comes from shear stresses set up in the cross-section of the sample. Torsion of a bar with length L and radius R is displayed in Figure 8. The internal resisting moment in the bar equals the twisting moment and can be written as

$$M_T = 2\pi \int_0^R \tau\, r^2\, dr \tag{15}$$

where τ is the shear stress, r is the radial distance to the center of the cross-section and R is the radius of the bar (Dieter, 1988, p. 341).

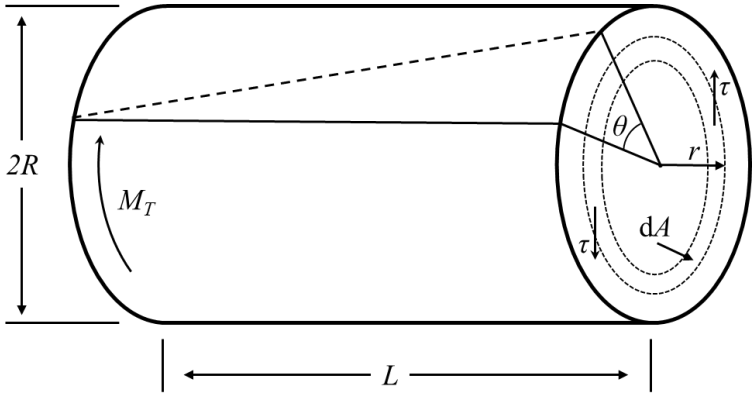

Figure 8 - Torsion of a cylindrical bar

From Figure 8 it is seen that the shear strain at distance r from the center of the cross-section and twist angle θ is

$$\gamma = \frac{r\theta}{L} \tag{16}$$

The shear strain rate follows from this equation

$$\dot{\gamma} = \frac{r}{L}\frac{d\theta}{dt} = \frac{r\omega}{L} \tag{17}$$

where ω is the angular velocity of rotation.

Nadai (1950) describes a method for calculating the shear stress at plastic deformation when the moment-twist curve is known. First, the unit shear is defined as

$$\gamma = r\theta' \tag{18}$$

where θ' is the twist per unit length, i.e. $\theta' = \theta/L$.

Assuming that the shear stress is a function of the shear strain, i.e. is given by the stress-strain curve in shear,

$$\tau = f(\gamma) \tag{19}$$

combining Equation 15, Equation 19 and Equation 18 gives

$$M_T = \frac{2\pi}{\theta'^3}\int_0^{\gamma_R} f(\gamma)\,\gamma^2\,d\gamma \tag{20}$$

$$M_T\theta'^3 = 2\pi\int_0^{\gamma_R} f(\gamma)\,\gamma^2\,d\gamma \tag{21}$$

where $\gamma_R = R\theta'$. Differentiating Equation 21 with respect to θ'

$$\frac{d}{d\theta'}M_T\theta'^3 = 2\pi R f(R\theta')\,(R\theta')^2 \tag{22}$$

Identifying that the maximum stress in the outer fiber of the bar is $\tau_R = f(R\theta')$ gives

$$\frac{d}{d\theta'}M_T\theta'^3 = 2\pi R^3\theta'^2\tau_R \tag{23}$$

Solving the derivation and rewriting for τ_R gives the following expression:

$$\tau_R = \frac{1}{2\pi R^3}\left[3M_T + \theta'\frac{\mathrm{d}M}{\mathrm{d}\theta'}\right] \tag{24}$$

At the maximum moment value M_{max}, the moment-twist curve is flat, i.e. $dM/d\theta' = 0$. From this follows that the maximum shear strain τ_{max} can be written as

$$\tau_{max} = \frac{3M_{max}}{2\pi R^3} \tag{25}$$

In Equation 24 it is assumed that the stress is independent of strain rate. For torsion testing at hot forming conditions, i.e. at $T = 0.6\,T_{melting}$, this is no longer valid. Dieter (1988, p. 346) gives the relation first statet by Fields and Backofen for the strain-rate dependence of flow stress at high temperature

$$\frac{\mathrm{d}M_T}{\mathrm{d}\theta'} = \frac{M_T}{\theta'}(m+n) \tag{26}$$

where m is the strain-rate sensitivity and n is the strain hardening exponent. At high temperatures, the strain-hardening effects generally become negligible, and can for practical purposes be ignored (Valberg, 2010). Combining Equation 24 and Equation 26 gives the maximum shear strain at a known maximum moment for hot deformation conditions when the strain hardening exponent is neglected

$$\tau_{max} = \frac{(3+m)M_{max}}{2\pi R^3} \tag{27}$$

The shear stresses and strains can be converted effective stresses and strains by multiplying with factors depending on the applied yield criterion. Kuhn and Medlin (2000) states the relationship between equivalent true stress and strain and shear stress and strain for the von

Mises criterion and the Tresca criterion. The equivalent true strain rate is derived from the equivalent true strain expressions. These relationships are as follows:

$$\bar{\sigma}_{eq} = \sqrt{3}\,\tau \tag{28}$$

Von Mises:

$$\bar{\varepsilon}_{eq} = \frac{\gamma}{\sqrt{3}} \tag{29}$$

$$\dot{\varepsilon}_{eq} = \frac{\dot{\gamma}}{\sqrt{3}} \tag{30}$$

$$\bar{\sigma}_{eq} = 2\tau \tag{31}$$

Tresca:

$$\bar{\varepsilon}_{eq} = \frac{2}{3}\gamma \tag{32}$$

$$\dot{\varepsilon}_{eq} = \frac{2}{3}\dot{\gamma} \tag{33}$$

The equivalent strain rate is derived from for Equation 29 and 32. A relationship between the strain rate and flow stress at constant temperature and strain is described in literature. For effective stress and strain rate, Dieter (1988, p. 297) states a relationship of the form

$$\sigma = C\dot{\varepsilon}^{m}|_{\varepsilon,T} \tag{34}$$

Where *C* is a material constant and *m* is the strain-rate sensitivity. This equation can be rewritten on the form $y = ax + b$, so that *m* becomes the slope of a linear line:

$$\ln\sigma = m\ln\dot{\varepsilon} + \ln C \tag{35}$$

The strain-rate sensitivity can hence be estimated from the slope of a $\ln\sigma$ vs $\ln\dot{\varepsilon}$ plot.

$$m = \frac{\partial \ln\sigma}{\partial \ln\dot{\varepsilon}} \tag{36}$$

From torsion test data, the strain-rate sensitivity *m* can be obtained by plotting $\ln\sigma$ vs $\ln\dot{\varepsilon}$ for constant strain and temperature. The slope of the best fit linear curve will then equal *m*.

2.5 Constitutive equations

Constitutive equations are material models that attempt to describe the flow of a given material (Valberg, 2010). These can be very useful when evaluating both cold and hot forming processes. In this thesis, constitutive equations related to hot forming will be considered.

2.5.1 Effect of temperature and strain rate on flow stress

The temperature and strain rate dependency on the flow stress is generally described to be a function of the Zener-Hollomon parameter presented in Equation 6 (Dieter, 1988, p. 307). For hot forming processes, the activation energy Q in Equation 6 is specified to be the activation energy for hot work Q_{hw} (McQueen & Ryan, 2002). Followingly, the Zener-Hollomon parameter is written

$$Z = \dot{\varepsilon} \exp\left(\frac{Q_{\mathrm{hw}}}{RT}\right) \tag{37}$$

When deformation occurs at steady-state conditions and the flow stress is constant, the relation between flow stress, strain rate and temperature can be modeled by an equation first described by Sellars and McTegart (1966):

$$\dot{\varepsilon} = A(\sinh(\alpha\sigma))^{n'} \cdot \exp(-Q_{\mathrm{hw}} \,/\, RT) \tag{38}$$

In Equation 38, sometimes called the Tagert-Sellars equation or the hyperbolic sine law, A, α and n' are constants. Rewriting to get an expression for the flow stress and combining it with Equation 37 gives

$$\sigma = \frac{1}{\alpha}\operatorname{arcsinh}\left(\frac{\dot{\varepsilon}\exp(Q_{\mathrm{hw}}/RT)}{A}\right)^{1/n'} = \frac{1}{\alpha}\operatorname{arcsinh}\left(\frac{Z}{A}\right)^{1/n'} \tag{39}$$

At low stress, i.e. at high temperatures and lower strain rates, this expression reduces to a power law:

$$\sigma = \left(\frac{\dot{\varepsilon}\exp(Q_{\mathrm{hw}}/RT)}{A_1}\right)^{1/n'} = \left(\frac{Z}{A_1}\right)^{1/n'} \tag{40}$$

In this relation, A_1 is a constant independent of A.

2.5.2 Fitting the parameters

Determining the constants in the constitutive relations can be done in several ways (McQueen & Ryan, 2002; Rønning, 1998; Shi, McLaren, Sellars, Shahani, & Bolingsbroke, 1997). Valberg (2010) suggests a method of curve fitting when the stress, strain rate and temperature are known. True stress is plotted for the natural logarithm of the Zener-Hollomon parameter, and the constitutive relations are made to fit the measured data by varying the constants. In addition to the constants in the constitutive relations, a particle contribution σ_b to the flow stress was included in the final equations, so that the flow stress $\sigma = \sigma_{costitutive} + \sigma_b$. This contribution takes into account the Orowan stress in Equation 5.

3 Material, experimental equipment and method

The experimental work carried out during this thesis work includes torsion testing at hot-working conditions, heat treatment of deformed samples between 355℃ and 560℃, sample preparation for light microscopy and light microscopy examination. All experimental work has been performed by the author at equipment located at the Department for Materials Science and Technology at NTNU. The torsion test procedure and equipment setup are partly based on earlier work at the department (Jensen, 2013, 2014; Langeng, 2002; Rist, 2016; Rønning, 1998).

3.1 The material

The sample material is an AA6082.54 alloy produced by Impol Aluminium Industries, Slovenia. The chemical composition of the alloy, as reported by the provider, is given in Table 2. The material is delivered to Raufoss Technology AS as extruded cylindrical workpieces of different dimensions. The sampled workpiece had a diameter of 79.9mm and length of 377mm.

Table 2 - Alloy composition

Element	Si	Fe	Cu	Mn	Mg	Cr	Zn	Ti	Cd	Hg	Pb	Al
wt%	1.30	0.21	0.08	0.55	0.91	0.17	0.02	0.02	0.0000	0.0002	0.003	rem

The workpiece was extruded from a billet with a diameter of 280 mm at an extrusion temperature of 520℃. The material was homogenized with a heating up to 540℃ over 2.5 hours and a holding time on 540℃ of 5 hours. It is reported that this material has Mn and Cr containing dispersoids with a mean size of 100 nm in an extent of about 30 dispersoids per μm^3 (Jensrud, 2018).

3.2 Torsion testing

The torsion setup and procedure will be described in this section. All torsion tests were performed on the material as-received, i.e. with no prior heat treatment, to a shear strain of 2π.

3.2.1 Torsion setup

The mechanical testing was performed using a hydraulically driven torsion setup, referred to as *the torsion machine.* An induction coil was used to heat the sample. A schematic layout of the torsion machine is displayed in Figure 9 and the actual machine is depicted in Image 1. The power unit of the machines is a hydraulic motor powered by a hydraulic pump. The rotation speed of the motor is determined by an electrically controlled valve that determines the hydraulic pressure in the system. Adjacent to the motor, an optical sensor records the rotation

of a holed disc mounted to the rod. The signal from the optical sensor is run through a computer program which controls the valve of the hydraulic motor. The motor is connected to a gear unit with a ratio of 1:19.5. This gear unit improves the process stability, but limits the maximum rotational speed to about 6 rad/s for the sample. The gear ratio was controlled prior to the testing.

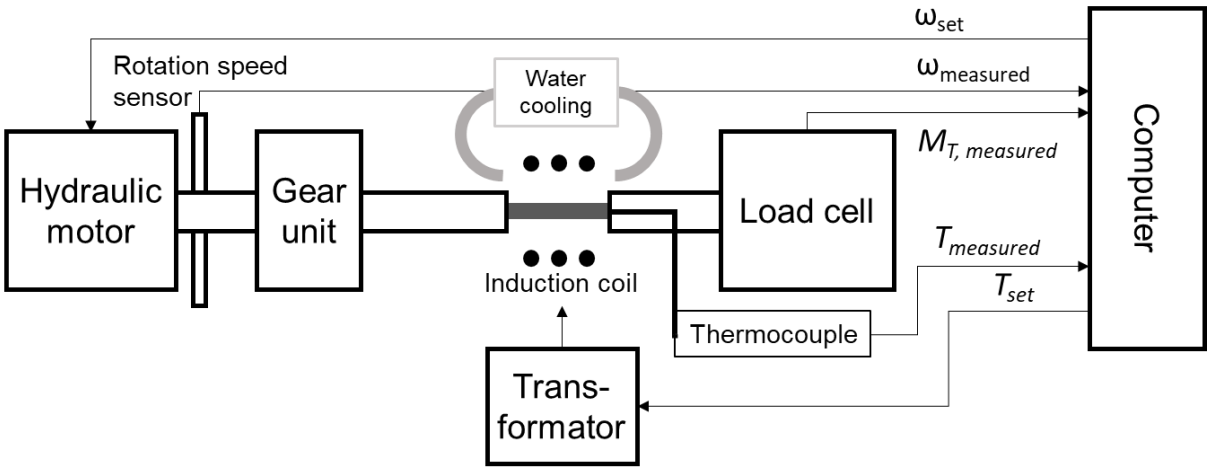

Figure 9 - Schematic presentation of the torsion machine.

The gear unit is connected to a second rod that is stabilized by a module visible in Image 1. The end of this rod is connected to the sample holder. On the other side of the sample, another sample holder is fastened to a third rod that is connected to a load cell. The load cell measures the moment, or torque, of this rod. These measurements are recorded by the computer. The load cell was calibrated and found to show measurements of consistently -0.15Nm below the calibrated value. A thermocouple measures the internal temperature of the sample. The

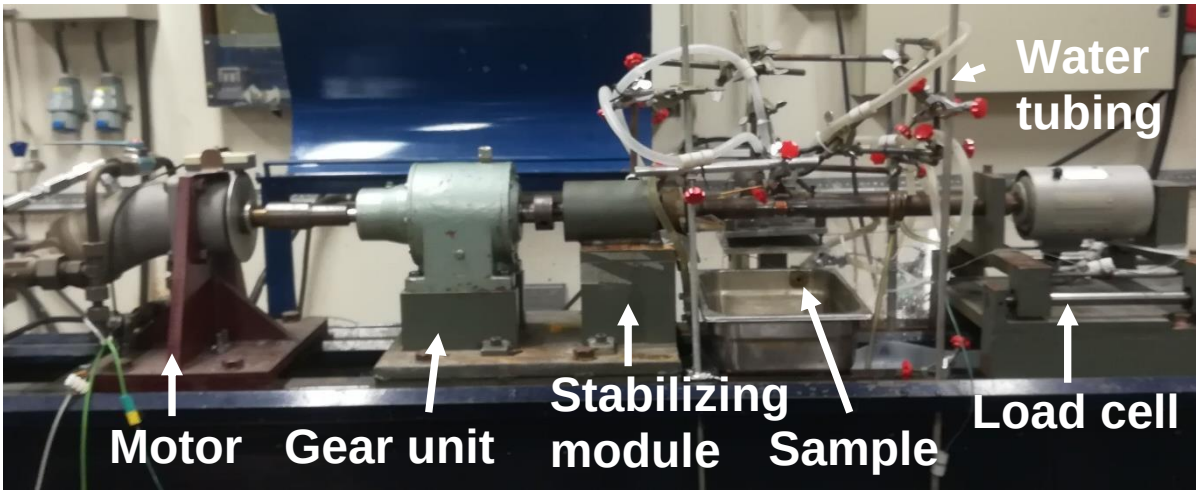

Image 1 – The torsion machine

temperature measurements are recorded by the computer and used to control the heating from the induction coil. A set of four similar water tubes connected to an electrical valve was used to quench the sample directly after deformation.

Image 2 displays the sample section of the machine. The thermocouple is inserted at one side of the sample, which is fastened between two sample holders by two screws on each side. The induction coil is positioned to cover but not touch the center section of the sample. This induction coil initially heated the sample at a rate of 15 K/s at 90% output. This rate decreased with increased temperature as the sample is cooled by mainly the sample holders (2.3 K/s at 400 ℃ was measured). The water tubes are positioned to hit the center of the sample.

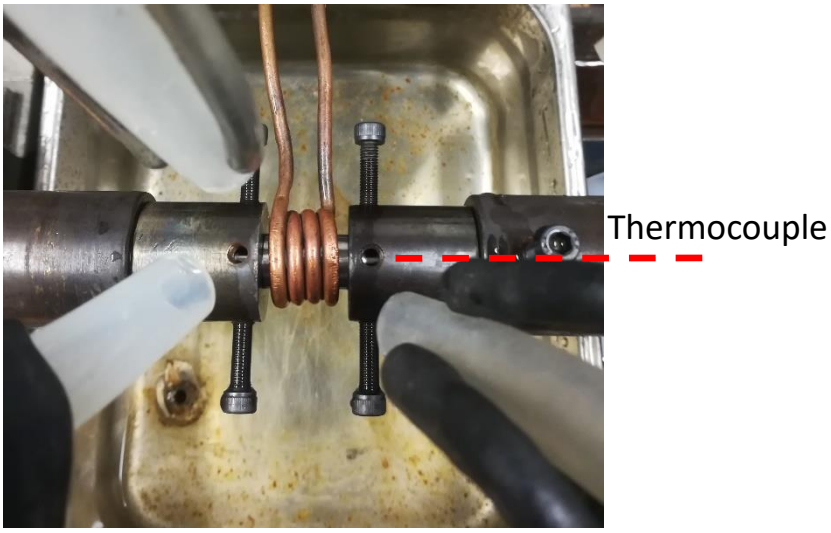

Image 2 – Close-up of the sample area .

3.2.2 Software

Both the process control and logging of results were carried out in a program made specifically for the torsion machine by previous users. The graphical software *National Instruments LabVIEW 2011* is the framework used for the program. The program uses a *Proportional Integral Derivative* (PID) controller to regulate both the rotation and the temperature. This controller is based on the minimizing the difference (e) between a given setpoint (SP) and a measured value (PV). A PID controller uses three elements, a proportional element (u_P), an integral element (u_I) and a derivative element (u_D), to set a controller output (u). Figure 10 shows an example of a PID-controller in LabVIEW. (National Instruments, 2018)

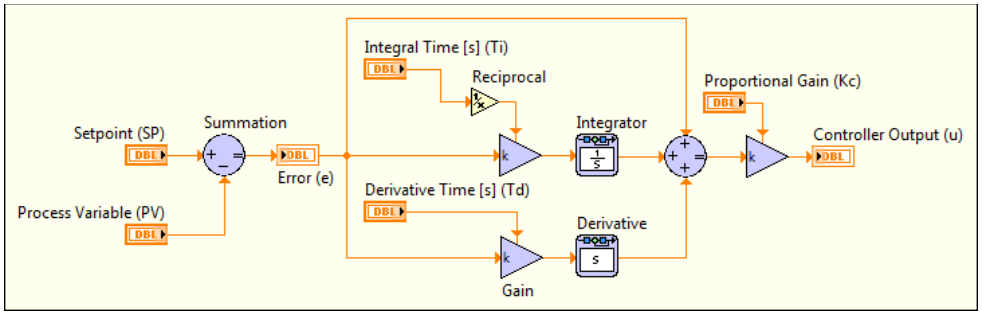

Figure 10 - Example of a PID-controller in *LabVIEW* (National Instruments, 2018).

The parameters of the PID-controllers were optimized by earlier users (Jensen, 2013; Rist, 2016).

3.2.3 Torsion samples

The torsion sample geometry was obtained from Rønning (1998). This geometry is displayed in Figure 11. The samples were machined by operators at the NT-faculty mechanical workshop. The larger parts on each side are for mounting the sample to the sample holder. A hole for insertion of a thermocouple was made on one side. The middle section of the sample is the test area. The dimensions of this section were measured to be within reasonable tolerances before testing and were found to be L = 10.00mm ± 0.01mm and D = 10.00mm ± 0.01mm. The edge at each end of the test section was made with a curvature of 0.2.

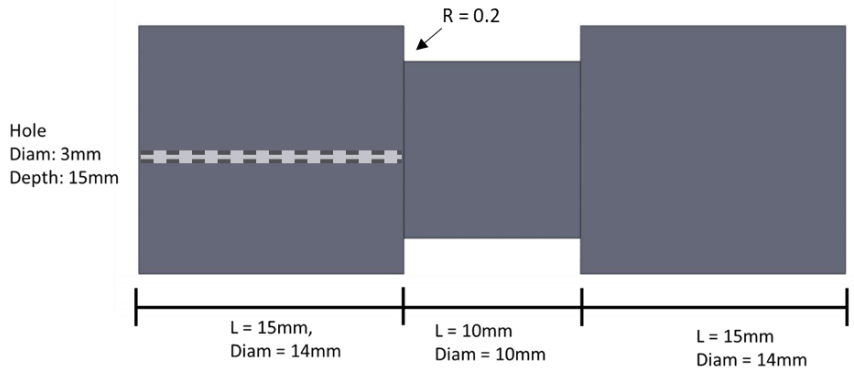

Figure 11 – An illustration of the geometry of the torsion sample with dimensions.

The samples were machined out of two extruded bolts provided by Raufoss Technology AS. The bolts have a cylindrical geometry with a length of 377mm and diameter of 80mm. Light microscopy examination of the microstructure of the bolts found that the structure consisted entirely of fibrous grains going lengthwise. The thickness of these grains was found to vary

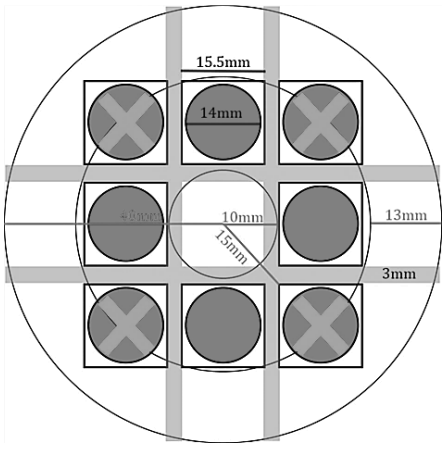

Figure 12 – Sample position in the cross-section of the bolt.

over the radius, with thicker grains (~200µm) in the center, very fine grains at the edge and medium thick grains halfway in between (~100µm). A plan for sample positions in the bolt was made, displayed in Figure 12, to ensure that the samples had similar microstructure. Two categories of samples retrieved with a slightly different radius from the center were initially planned, but only one of these was machined to final samples (samples marked with an X in Figure 12 were discarded). Samples were taken from the whole length of the bolt, and each bolt yielded about 30 samples.

3.2.4 Testing procedure

The torsional tests described in this thesis were carried out in multiple sessions over about 3 months. Initially, a small trial was done to find a suitable testing procedure and certify that the samples could be analyzed using light microscopy.

A rotation of 4π radians was chosen for all tests. The rotational speed was varied by inserting the target value into the control program. All samples were heated with the same heat output up to a target temperature, and the temperature was kept constant during deformation. The motor was started within 5 sec. of reaching the target temperature. The samples were automatically quenched and cooled down to room temperature directly after deformation. Special care to avoid additional deformation was taken when the samples chosen for further investigation were removed from the sample holders. This was done to avoid accidentally influencing the microstructure. Data files of temperature, rotation, rotational speed and moment were made for all the test. *Microsoft Excel* was used to organize and analyze the gathered data.

3.2.5 Heat treatment

The heat treatment of the deformed samples aimed at emulating an industrial *solution heat* treatment process. To prepare samples for heat treatment, the ends of the torsion test samples were cut off using a *Struers Accutom-5* disc cutter. Then, each sample was cut into four wedge-shaped parts, as illustrated in Figure 13. Finally, the samples were engraved for identification and attached to a steel string for safe handling.

Preheated salt baths were used for the heat treatment. The desired temperature was set for each of the six baths available and then measured with a separate thermoelement. Temperatures ranging from 355°C to 560°C were used. The variation in temperature was within ± 2°C of the set temperature, measured before the sample was inserted and after it was removed. Each

sample was heat treated for 15 minutes before it was immediately quenched in a water bath. Due to their small sizes, it is assumed that the samples were instantly heated and cooled without any temperature gradients.

3.2.6 Metallography

A standard metallographic sample preparation procedure was used to prepare the samples for light microscope examination. First, four and four samples were molded into epoxy. Then, about 1 mm was removed from the samples by grinding, as illustrated in Figure 13. The surfaces were then manually grinded in steps to 4000 ASTM MESH fineness and automatically polished at 9 µm, 3 µm and 1 µm in a *Struers Tegramin-30* automatic polishing machine. The samples were thoroughly cleaned and anodized with a 5% HBF_4-solution for 90 sec. at 20.0 volts.

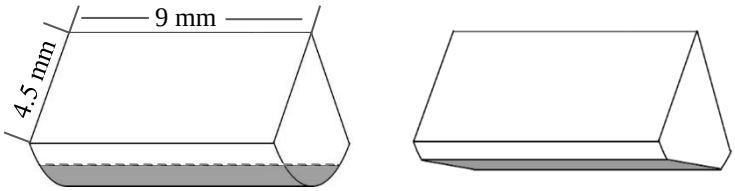

Figure 13 – Illustration of the grinded area and sample geometry.

A *Leica Axio Vert.A1* microscope with polarized light was used for the examination. An accompanying software named *ZEN Core* was used to gather images.

4 Experimental Results

The results from the torsion tests and light microscopy analysis are presented in this section.

4.1 Rotational speed

Plot 1 presents a selection of measured rotational speeds in rad/s of the sample at preset rotational speeds of 6 rad/s, 2 rad/s and 0.2 rad/s. Five tests were performed for each rotational speed, all at different deformation temperatures. The temperatures plotted is 350, 400, 450, 500 and 550 ℃. The average of the rotational speed data for each test was used in further calculations. Appendix A lists the average rotational speeds with standard deviation for all the torsion tests.

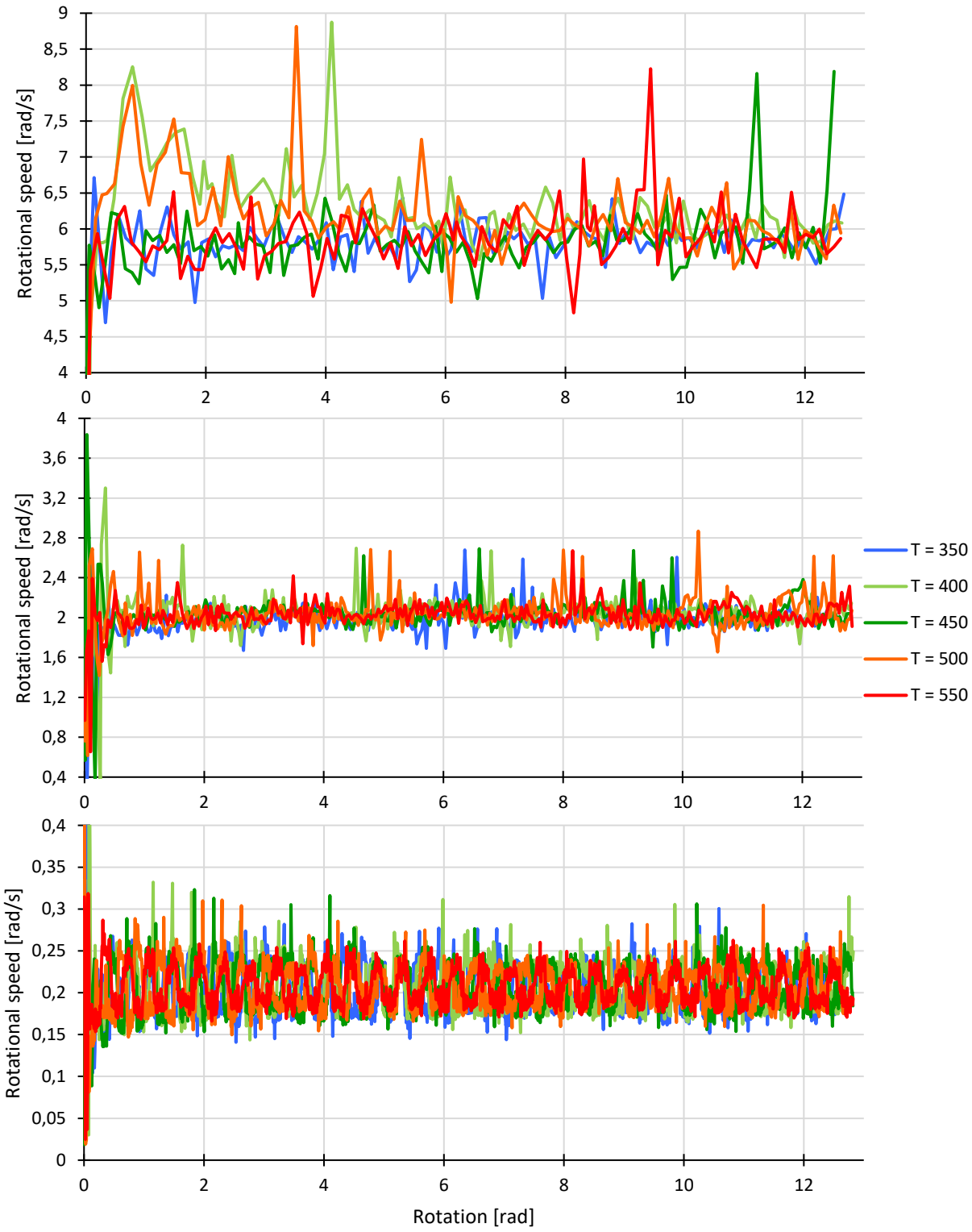

Plot 1 – Measured rotational speed in rad/s for preset rotational speeds of 6 rad/s, 2 rad/s and 0.2 rad/s (top to bottom).

4.2 Torque

In this section, a selection of measured torque [Nm] data for three different rotational speeds, each with five different deformation temperatures, are plotted against rotation [rad]. The temperatures are 350, 400, 450, 500 and 550 °C. All tests stopped after 4π rad, corresponding to a final strain of γ = 6.28. The rotational speed in Plot 2, Plot 3 and Plot 4 are 0.2 rad/s, 2 rad/s and 6 rad/s, respectively. The maximum moment was found by taking the average of a set of data adjacent to the peak of the torque curve. All these values are listed in Appendix A accompanied by the standard deviation of the chosen data set. Note: All tests are measured with the same recording frequency. The number of data points will therefore decreases with increasing rotational speed.

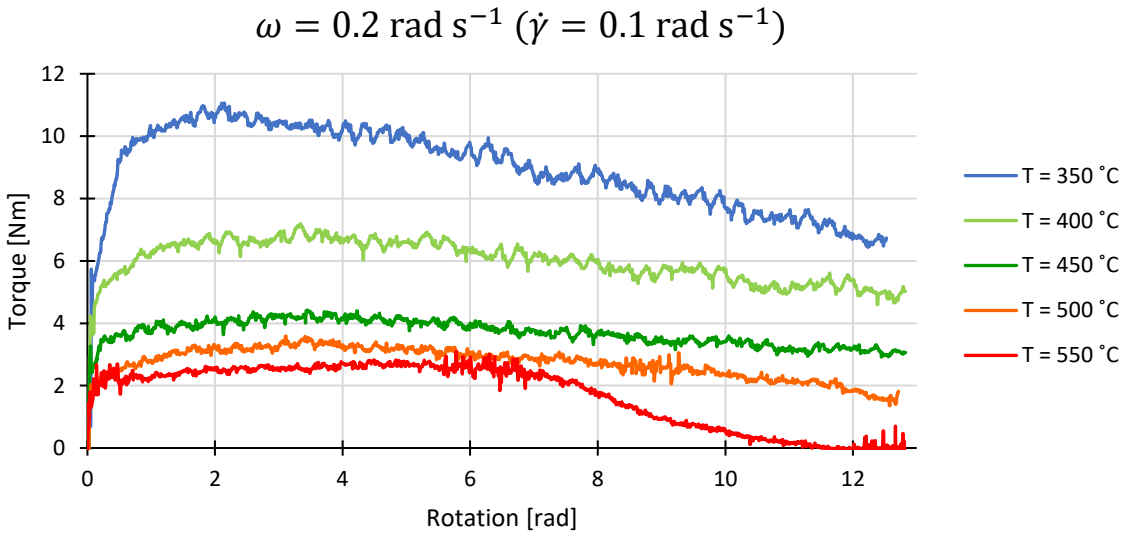

Plot 2 – Torque [Nm] vs. rotation [rad] for torsion tests at a rotational speed of 0.2 rad/s.

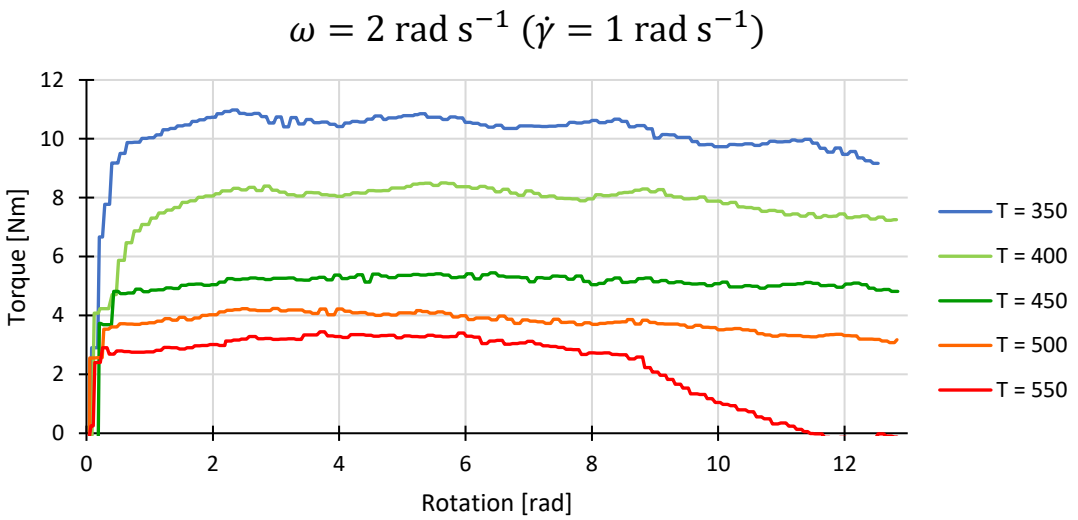

Plot 3 - Torque [Nm] vs. rotation [rad] for torsion tests at a rotational speed of 2 rad/s.

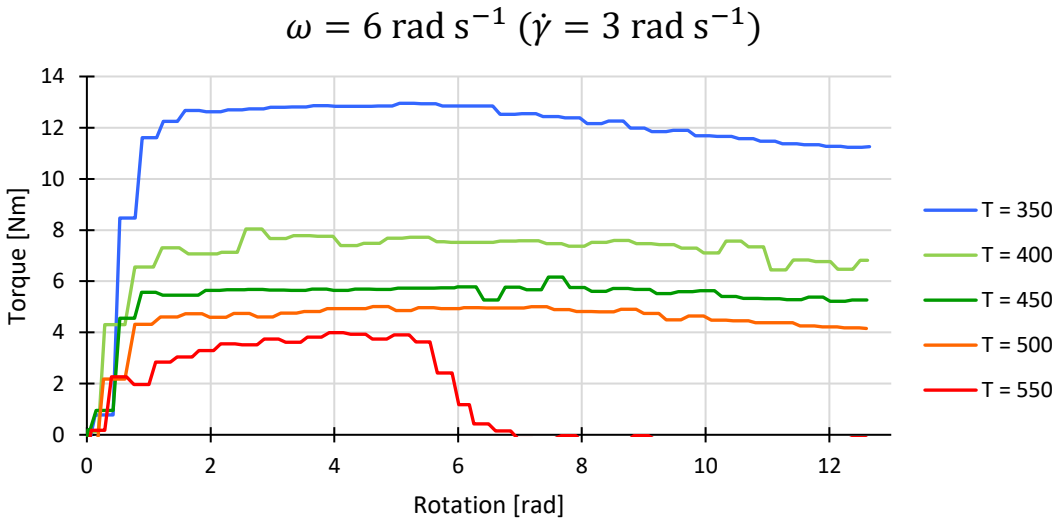

Plot 4 - Torque [Nm] vs. rotation [rad] for torsion tests at a rotational speed of 6 rad/s.

It was observed that some of the samples that were deformed at 550 ℃ fractured during torsion. This is supported by the rapid decrease in torque of the 550 ℃ curves about halfway into the test.

4.3 Maximum moment vs deformation temperature

A selection of maximum moment values sampled from the torque measurements is plotted for deformation temperature [°C] for different rotational speeds in Plot 5. The plotted data are listed in Appendix A. It is apparent that the steepness of the slope decreases with increasing temperature. An exponential trend line marks the observed trend.

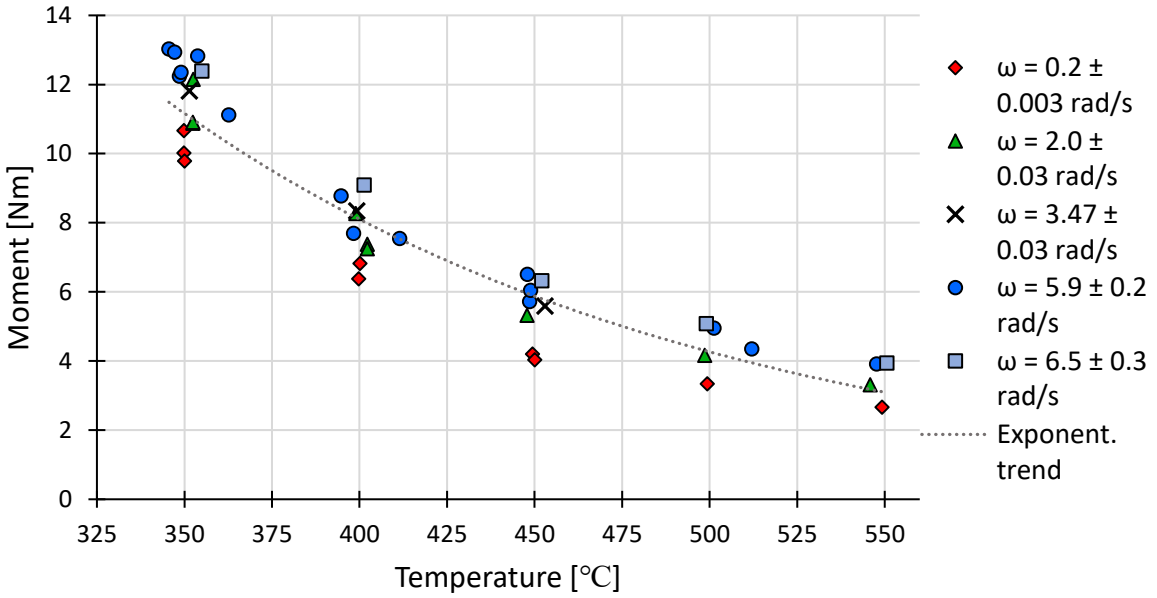

Plot 5 – Maximum moment [Nm] vs deformation temperature [°C] for different rotational speeds [rad/s]. An exponential best fit curve is included to highlight an apparent trend.

4.4 Strain rate sensitivity

Plot 6 displays the true stress and true strain values used to calculate the strain-rate sensitivity *m*. First, *m* was set to zero and the true stress was calculated from maximum moment values using Equation 27 and 28. The true strain was calculated using Equation 17 and 30. When a new *m*-value was calculated, the *m* in Equation 27 was updated and the calculation repeated until the *m*-value stabilized. Three iterations for *m* were made before the value stabilized on the values given in Table 3. All *m*-values are listed in Appendix B. For samples deformed at temperatures other than the ones listed in Table 3, a weighted average interpolation was used to estimate the *m* value.

Table 3 – Strain-rate sensitivity for the sample material at given temperatures.

$T_{Deformation}$ [°C]	350	400	450	500	550
m	0.062	0.071	0.118	0.118	0.115

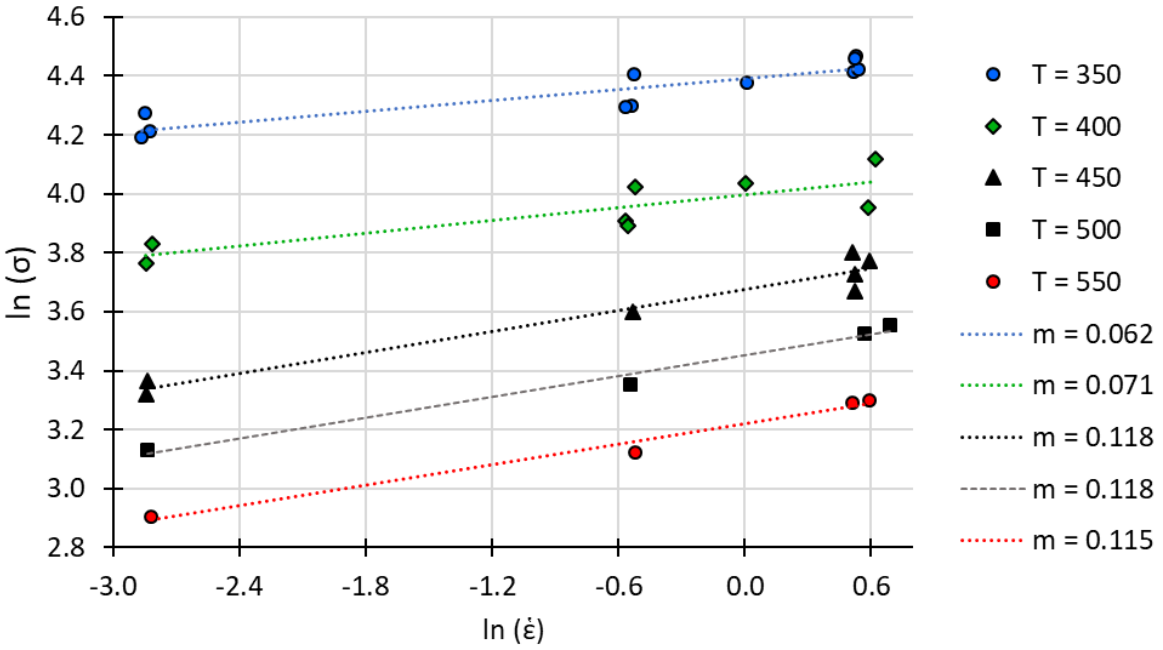

Plot 6 – Natural logarithm of true stress plotted vs. natural logarithm of true strain. The slope of the linear best fit curves is the strain-rate sensitivity *m* at the given deformation temperature.

4.5 Constitutive relations

The results from the curve fitting described in section 2.5.2 are presented in this section. Plot 7 displays the experimental true stress value plotted for the natural logarithm of the experimental Zener-Hollomon parameters. Equation 39 and 40 are fitted to the data by varying the constants to minimize the error between the experimental results and the calculated values. Table 4, Table 5 and Table 6 gives the constants of the Zener-Hollomon parameter, Power law and Hyperbolic sine law (Sinh law) respectively.

Table 4 – Constants in the Zener-Hollomon parameter (Equation 37)

$Z = \dot{\varepsilon} \exp\left(\frac{Q_{\mathrm{hw}}}{RT}\right)$	
R [J/ mol K] (Blackman, 2014)	Q_{hw} [kJ/mol] (manually fitted)
8.31446	170

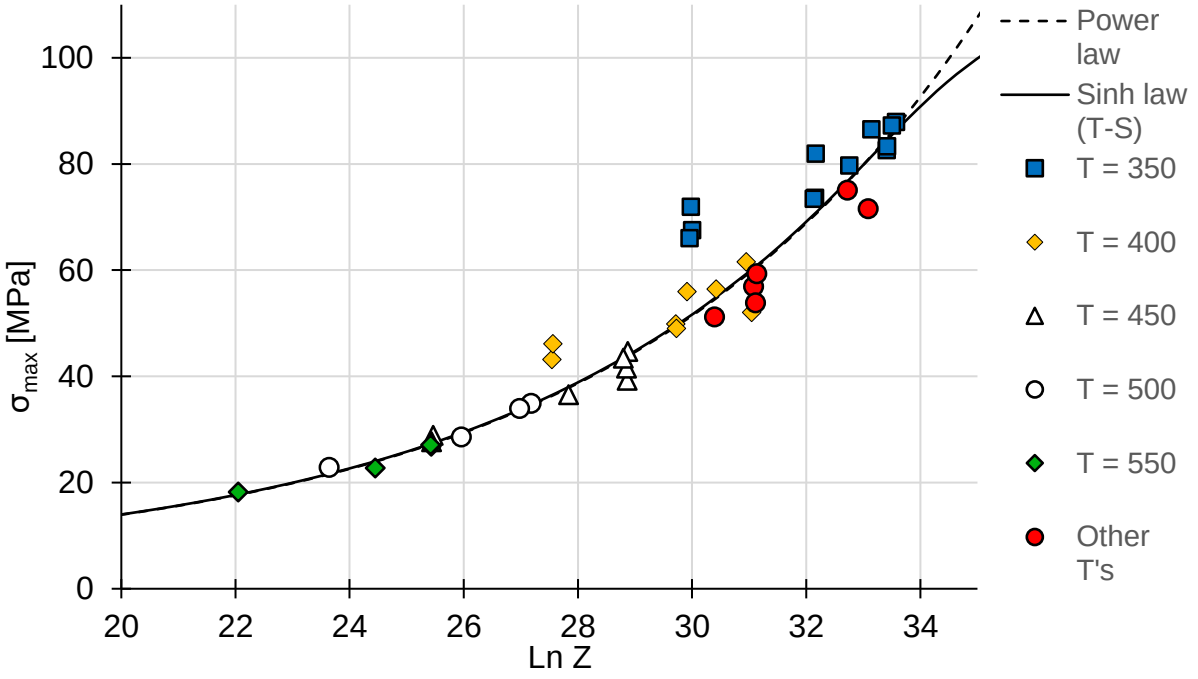

Plot 7 – The measured maximum true stress [MPa] plotted for the natural logarithm of the measured *Z*-values for an activation energy Q_{hw} = 170 kJ/mol. Table 5 gives the equation for the Power law curve. Table 6 gives the equation for the Sinh law curve.

Table 5 – Calculated constants in the Power law (Equation 40)

$\sigma = \left(\frac{\dot{\varepsilon}\exp(Q_{hw}/RT)}{A_1}\right)^{1/n'} + \sigma_b$			
Q_{hw} [kJ/mol]	σ_b [MPa]	A_1 [s^{-1}]	n'
170	4	200.0	6.4

Table 6 – Calculated constants in the hyperbolic sine law (Equation 39)

$\sigma = \frac{1}{\alpha}\operatorname{arcsinh}\left(\frac{\dot{\varepsilon}\exp(Q_{hw}/RT)}{A}\right)^{1/n'} + \sigma_b$				
Q_{hw} [kJ/mol]	σ_b [MPa]	α [1/MPa]	A [s^{-1}]	n'
170	4	0.0115	5.01E+14	6.4

4.6 Metallographic images

In this section, a selection of metallographic images is presented. A total of 56 samples was depicted in order to categorize the microstructure. It was found that the microstructure after heat treatment could be divided into 4 categories briefly described in Table 7. Image 3 depicts the microstructure of the sample prior to deformation. The image includes the whole cross-section of the sample in the extrusion direction, i.e. from edge to edge through the center. The structure shows a fibrous structure. OED identifies the original extrusion direction.

It is observed that the recrystallized grains are longer in the shear direction, i.e. approximately perpendicular to the original extrusion direction. The size of the grains is therefore measured as two parameters. *D* is the maximum length of the largest grain and *H* is the thickness of this grain.

Table 7 – Description of the microstructure categories

Structure, category	Example image	Description
Deformed fibrous	Image 4	The structure shows no sign of equiaxed grains. The observed grains are very fine and show an elongation in the shear direction.
Mixed structure	Image 8, Image 9	The structure consists mainly of deformed fibrous grains, but a few large grains are observed. The structure can also be ambiguous.
Recrystallized, small grains	Image 5	The structure consists of relatively equiaxed grains with *D* between 200µm and 500µm. *H* varies between *D*/4 and *D*/2.
Recrystallized, medium grains	Image 6	The structure consists of grains with *D* between 500µm and 1500µm. *H* varies between *D*/5 and *D*/3 for each structure.
Recrystallized, large grains	Image 7	The structure consists of grains with *D* between 1500µm and the width of the polished surface (~3800µm). *H* varies between *D*/9 and *D*/4 for each structure.

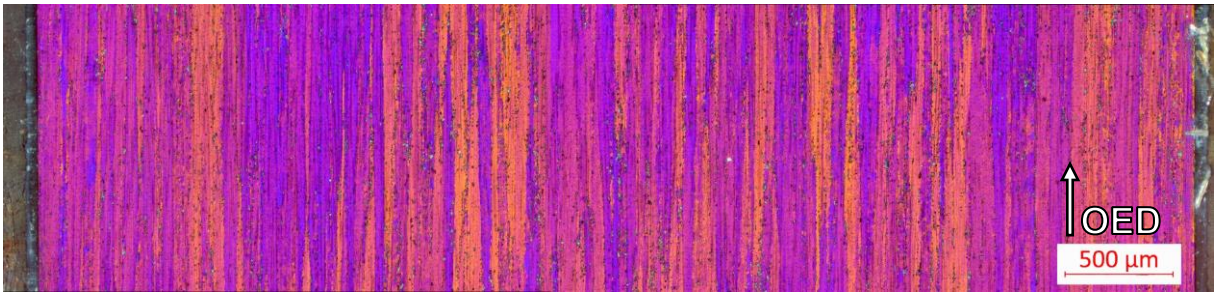

Image 3 - Undeformed sample. Image shows the whole cross-section.

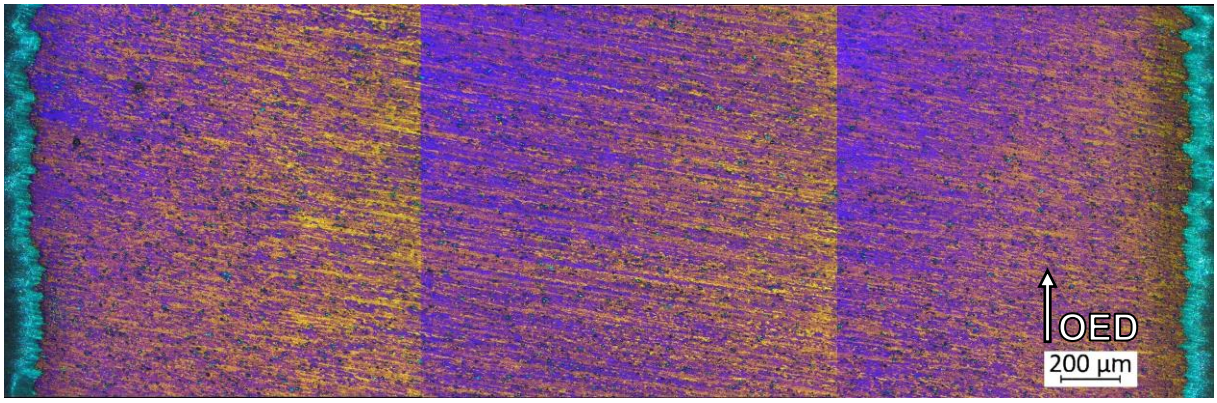

Image 4 - Deformed fibrous grains. $Z = 1.58 \times 10^{13}$, $T_{\text{Heat treatment}} = 490°C$

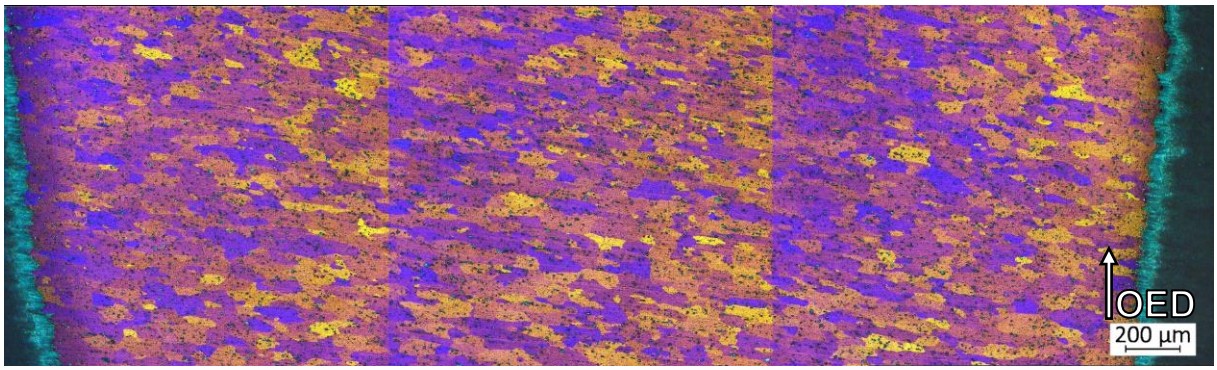

Image 5 - Recrystallized, small grains. $Z = 3.24 \times 10^{14}$, $T_{\text{Heat treatment}} = 520°C$

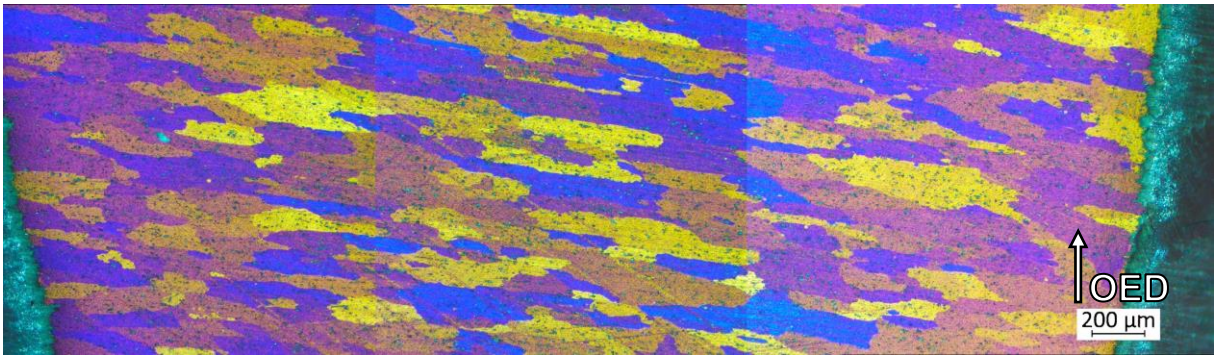

Image 6 - Recrystallized, medium grains. $Z = 3.24 \times 10^{14}$, $T_{\text{Heat treatment}} = 430°C$

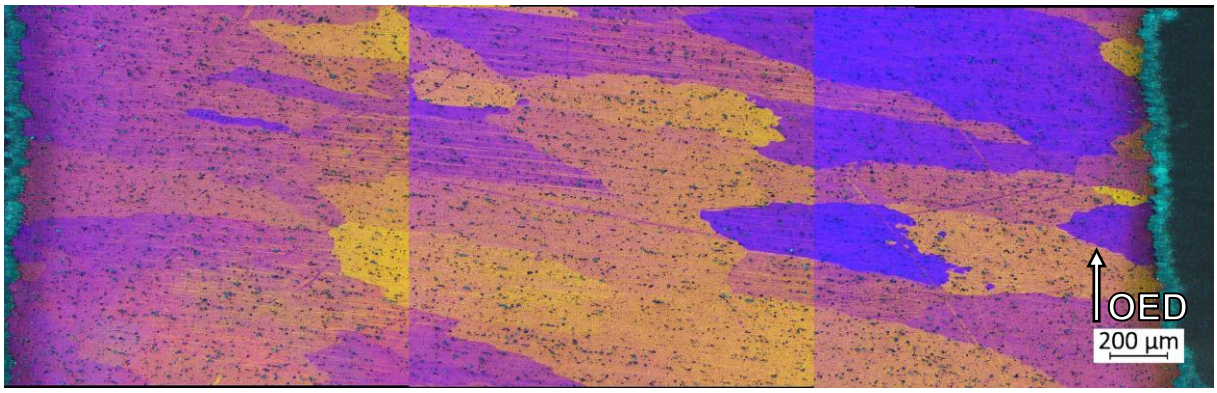

Image 7 - Recrystallized, large grains. $Z = 3.46 \times 10^{12}$, $T_{\text{Heat treatment}} = 530°C$

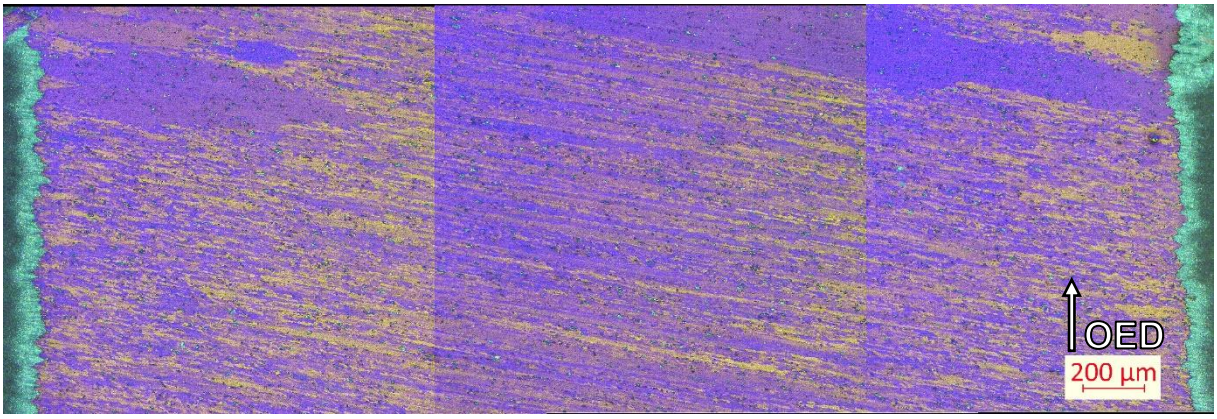

Image 8 – Mixed structure. Some large recrystallized grains are observed at the top of the image. $Z = 1.69 \times 10^{12}$, $T_{\text{Heat treatment}} = 539°C$

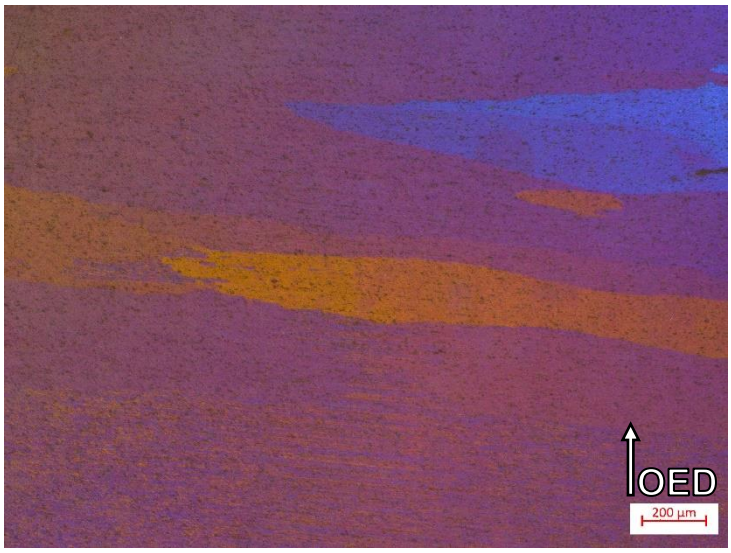

Image 9 – Mixed structure. Deformed fibrous grains (bottom) with a sharp transition to large recrystallized grains (middle and top). $Z = 1.68 \times 10^{14}$, $T_{\text{Heat treatment}} = 398°C$

4.7 Recrystallization

Plot 8 presents the observed microstructure after deformation with a recorded Zener-Hollomon parameter Z and a heat treatment at a given temperature. Two lines are included in the plot to mark an apparent transition from a microstructure with deformed fibrous grains to a recrystallized structure. The lines are conservative estimates mainly meant for practical purposes. Table 8 presents the equations of these lines.

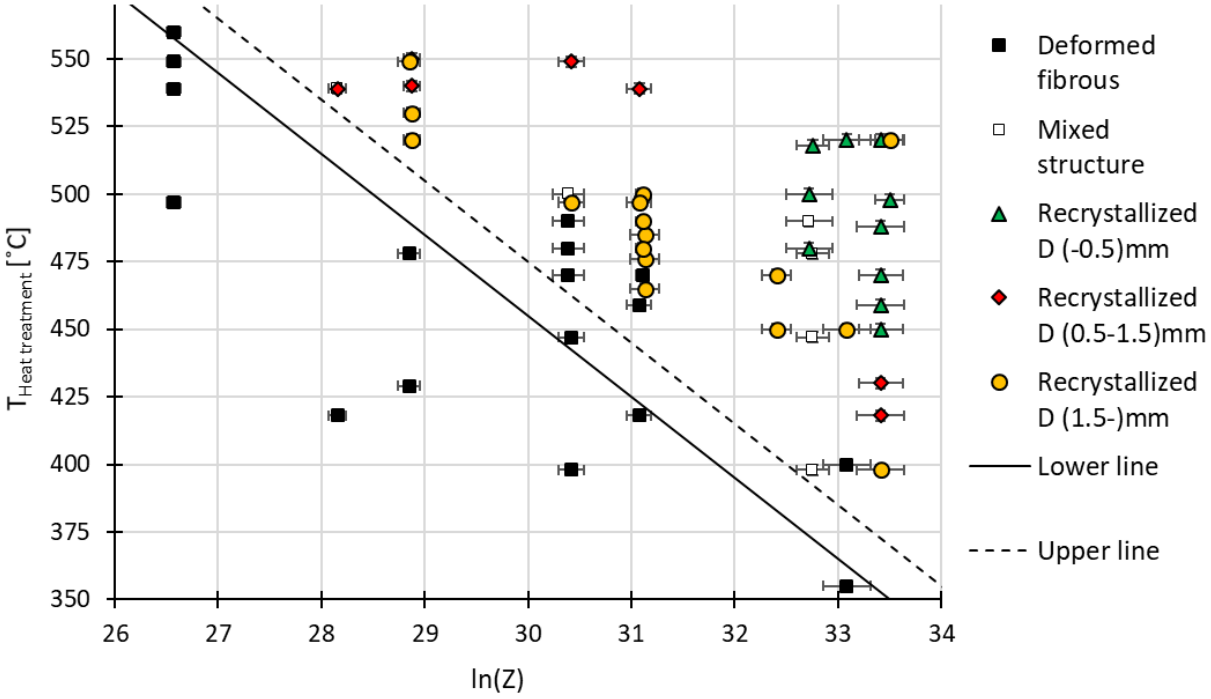

Plot 8 - Observed microstructure after heat treatment at a given temperature [°C] after deformation with a measured Zener-Hollomon parameter. A lower and upper line are drawn to mark an apparent transition from deformed fibrous structure to a recrystallized structure.

Table 8 – Deformed structure – recrystallized structure boundary expressions.

Lower line	$T\ [°C] = 1355 - 30 \times \ln Z$
Upper line	$T\ [°C] = 1375 - 30 \times \ln Z$

5 Discussion

In the following section, the experimental results and their accuracy will be discussed. In addition, the practical implication of the results will be debated.

5.1 Flow data

5.1.1 Rotational speed

The curves of the rotational speeds presented in Plot 1 show that the variance in the data set increases with increasing rotational speed. The data also oscillate around a mean value. Both these effects are likely due to the regulation of the system. This led to some instability on the strain rate measurements at high rotational speeds.

5.1.2 Torque data

It can be seen from Plot 2, Plot 3 and Plot 4 that the measured torque data follows an expected trend. The difference in slope of the curve after the maximum suggests different rates of dynamic softening at different temperatures, results also found for 7075 aluminum (Quan, Liu, Zhou, & Chen, 2009). The torque increases with decreasing temperature at a constant rotational speed. The maximum moment plotted for deformation temperature in Plot 5 shows that the torque decreases with decreasing strain rate at constant temperatures.

5.1.3 Strain rate sensitivity

The results in Section 4.4 shows that the strain rate sensitivity increases with increasing deformation temperature up to 500℃. An unexpected decrease is seen from 500℃ to 550℃. This may be seen in correlation to the fracture of the samples at 550℃. A possible explanation is the presence of intermetallic phases with low melting points. Ponweiser, Lengauer, and Richter (2011) reports that the eutectic temperature of the Al_2Cu phase (θ-phase) approximately 550℃. The tested material contains 0.08 wt% Cu, and is unlikely to form Al_2Cu-phase. Further investigation should be carried out before any conclusions can be made.

5.2 Activation energy and constitutive relationships

A recently published paper by Ren, Xu, Chen, and Qin (2018) investigated an AA6082 with an alloy composition similar to the alloy investigated in this thesis. In this paper, an activation energy of $Q = 174.9\ \mathrm{kJ/mol}$ for $\alpha = 0.0269\ \mathrm{MPa^{-1}}$ was reported. An alternative method of estimating the activation energy was applied by these authors, finding Q by plotting

$\ln(\dot{\varepsilon})$ vs. $\ln(\sinh(\alpha\sigma))$ and $\ln(sinh(\alpha\sigma))$ vs. $1/\mathrm{T}$. Q can then be calculated by the following expression

$$Q = R\left(\frac{\partial \ln \dot{\varepsilon}}{\partial \ln(\sinh(\alpha\sigma))}\right)_T \times \left(\frac{\partial \ln(\sinh(\alpha\sigma))}{1/T}\right)_{\dot{\varepsilon}} \qquad (41)$$

This method was also tried for the experimental data in this thesis. Because of inconsistencies in the measurements, a single Q value could not be deduced from this method. This suggests that the stability of the test method may be an issue.

It is seen in Plot 7 that the stress values for low *Z*-values fit well with the constitutive relationships. At higher *Z*-values, the measured stress values deviate markedly from the estimated relationships. Especially at low strain rates ($\dot{\gamma} = 0.1\ \mathrm{s}^{-1}$) for deformation temperatures of 350°C and 400°C. According to the estimated relations, the true stress at $\dot{\gamma} = 0.1\ \mathrm{s}^{-1}$ and $T = 350$°C should be about 20 MPa lower than the measured value. On the other hand, the relations seem to correlate well with measured stress at higher temperatures and strain rates. This implies that the Zener-Hollomon less suitable for describing deformation with low strain rate ($\dot{\gamma} < 1\ \mathrm{s}^{-1}$) at temperatures in the lower end of the hot working range (~ 0.6 T_{melting}). It may also imply that the dynamic softening come from different mechanisms at lower temperatures.

The constitutive relations seemingly correspond well, with one exception, with the experimental results for Zener-Hollomon parameters between 3.75×10^9 and 3.45×10^{12}. For Zener-Hollomon parameters between 3.45×10^{12} and 3.8×10^{14}, the equations only partly corresponded with the experimental data, with large deviations for low strain rates at lower temperatures. Performing tests with *Z* values within this range, but with higher temperatures and strain rates could give more insight into this trend. It is believed that these measurements would correspond better with the constitutive equations. More sophisticated testing equipment is a requirement to achieve this.

5.3 Recrystallization

Section 4.6 shows that the resulting microstructure after deformation and heat treatment vary greatly depending on the Zener-Hollomon parameter and the heat treatment temperature. It is evident that the material in some cases has undergone recrystallization. Some samples also show evidence of secondary recrystallization. More investigation should be done to better

understand the mechanisms taking place in the material. Particle stimulated nucleation is known to take place in aluminum during heat treatment after deformation (Humphreys & Hatherly, 2004). On the other hand, dynamic recrystallization has been reported to take place in AA6082 aluminum (Ren et al., 2018). Equation 14 states that the critical strain for geometric dynamic recrystallization is dependent on *Z*. If the constants in the equation were known, the critical strain could be calculated to give an estimate of the plausibility of geometric dynamic recrystallization.

It is seen in Section 4.7 that the recrystallized grains have different size. From Plot 8 it is also seen that the grain size shows a dependency on the *Z*-value. Small grains are only seen at high heat treatment temperatures at high *Z*-values. Large grains are seen for *Z*-values or heat treatment temperatures lower than for the small grains. This observation has been summarized and is presented in Figure 14.

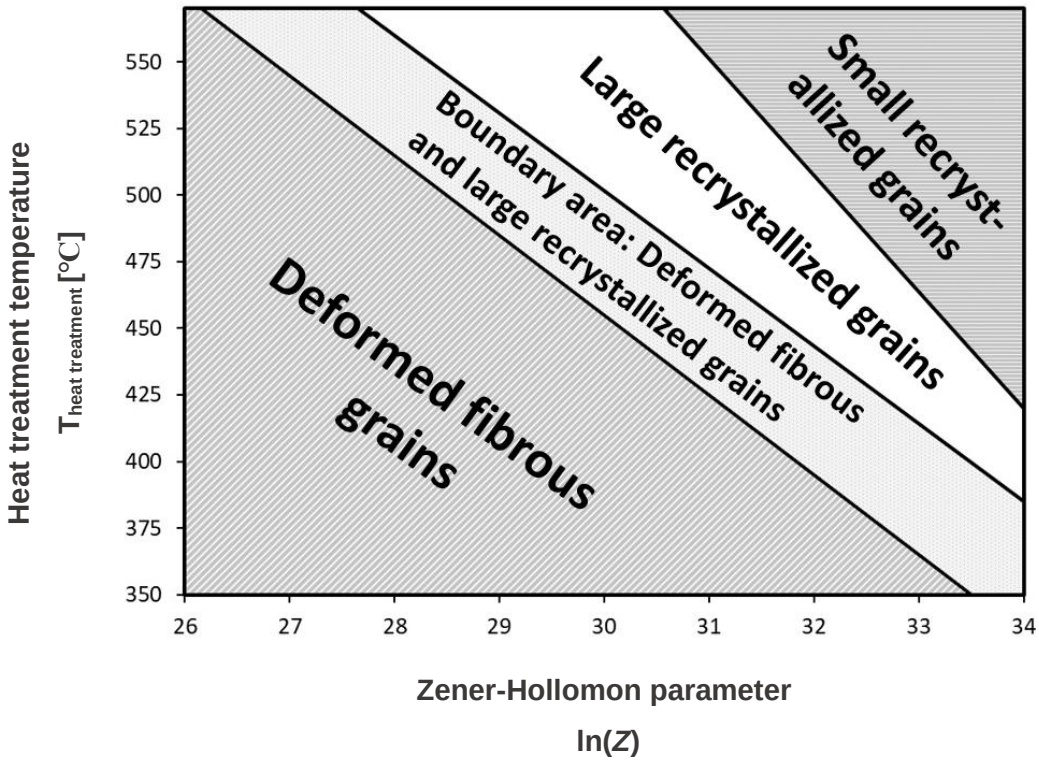

Figure 14 – A summary of the microstructures seen after heat treatment.

It can be argued that the difference in grain size comes from the number of nucleation sites for recrystallized grains. The critical radius of a nucleus to become a recrystallized grain is presented in Section 2.3.2.1. This is said to be dependent on the driving pressure from deformation P_D and the retarding pressure from fine particles, so-called Zener-pinning, P_Z. It is

shown that the critical radius decreases with increasing P_D, meaning more nuclei will become recrystallized grains. In Section 2.3.1, it is stated that the stored deformation is dependent on the Zener-Hollomon parameter. A probable explanation is hence that higher Zener-Hollomon parameters causes more nuclei to form recrystallized grains, creating a stable microstructure with more, and therefore smaller, grains.

The mechanism of the observed recrystallization could not be deduced based on the light microscope images alone. Further investigation could give more insight into the driving mechanisms.

5.4 Practical implementation

The results in this thesis are likely to have some practical value. Computer simulations have become an important and cost-saving tool in modern industry. The latest *final element modeling* (FEM) software can be made to simulate flow data and temperature in an industrial metal forming process with relative ease and precision. The simulation of microstructure evolution is on the other hand very complex and time-consuming. By implementing the results from Section 4.7 into a FEM code, the flow and temperature simulations can be used to estimate the final microstructure after heat treatment. This can give valuable information about areas with risk of recrystallization during a design process. Hopefully, this can help save time, money and resources by reducing the need for trials and prototyping.

Additionally, the constitutive relationships in Section 4.5 can potentially be implemented in a FEM code and help to improve the flow simulations for the AA60882.54 alloy.

5.5 Accuracy of the results

5.5.1 Instability of rotational speeds

As discussed in Section 5.1.1, the torsion machine suffered from instability at high rotational speeds. This led to a relatively large variance in the highest strain rate measurements compared with the lower strain rates. This made keeping a constant strain rate difficult and unpredictable.

5.5.2 Change in sample geometry

Preliminary torsion testing at low rotational speeds and high temperatures showed no significant change in the sample geometry. This was hence assumed to be negligible. After testing at high

Z-values, some of the samples showed signs of a localized cross-section reduction higher than first assumed. The largest reduction measured was approximately 2.5 percent after a shear strain of 2π. This observation was not included in this thesis, but could help improve the accuracy of future work.

5.6 Further work

Suggested future work includes:

- Reproduction of the torsion tests in a more sophisticated torsion machine could both allow for higher Zener-Hollomon parameters and a process with less varying measurements.
- Reproducing the torsion tests with controlled sample geometry.
- Texture analysis of the deformed and recrystallized microstructure could help deduce the driving mechanism of recrystallization.
- In-situ annealing of a deformed sample in EBSD could give further insight in the recrystallization of the alloy.

6 Conclusion

An AA6082.54 aluminum alloy used in the production of car suspension components was evaluated in terms of flow properties and recrystallization. The flow properties of the material during hot working conditions were examined by torsion testing. Constitutive relationships were estimated from the experimental results. The activation energy for hot work for the alloy was found to be Q_{hw} = 170 kJ/mol. It was seen that the experimental results deviated from the models at low strain rates and low deformation temperatures (~0.6 $T_{melting}$). Two constitutive equations were suggested based on curve fitting to experimental results. It was found that the flow stress could be modeled with the power law form of the Tegart-Sellars equation with the material constants $A_1 = 200.0\ s^{-1}$, $n' = 6.4$ and a dispersoid hardening contribution $\sigma_b = 4$ MPa. The hyperbolic sine form of the Tegart-Sellars equation was found to have the material constants $A = 5.01 \times 10^{14}\ s^{-1}$, $\alpha = 0.0115\ MPa^{-1}$, $n' = 6.4$ and $\sigma_b = 4$ MPa. These equations seemingly correspond well, with one exception, with the experimental results for Zener-Hollomon parameters between 3.75×10^9 and 3.45×10^{12}. For Zener-Hollomon parameters between 3.45×10^{12} and 3.8×10^{14}, the equations only partly corresponded with the experimental data, with large deviations for low strain rates at lower temperatures.

Additionally, it was found that the material was susceptible for primary and secondary recrystallization during heat treatment after deformation. The material was tested for heat treatment temperatures between 355℃ and 560℃ after torsion to a shear strain of 2π with Zener-Hollomon parameter between 3.45×10^{11} and 3.54×10^{14}. A linear relationship between as-deformed and recrystallized microstructure was suggested. It was found that there was a risk of recrystallization during heat treatment when the temperature is above $T\ [℃] = 1355 - 30 \times \ln Z$, where Z is the Zener-Hollomon parameter for the deformation.

7 References

The Aluminium Automotive Manual. (2002). Retrieved from https://www.european-aluminium.eu/resource-hub/aluminium-automotive-manual/

Amado, M. N., & Daroqui, F. (2015). Revision of The Solvus Limit of Al-Mg2Si Pseudo Binary Phase Diagram. *Procedia Materials Science, 8*, 1079-1088. doi:https://doi.org/10.1016/j.mspro.2015.04.171

Blackman, A. G. (2014). *Aylward and Findlay's SI chemical data/*
Allen Blackman; Lawrence Gahan (7th edition ed.): John Wiley & Sons Australia, Ltd.

Dieter, G. E. (1988). *Mechanical Metallurgy*: McGraw-Hill Book Company Ltd.

Du, Q., Tang, K., Marioara, C. D., Andersen, S. J., Holmedal, B., & Holmestad, R. (2017). Modeling over-ageing in Al-Mg-Si alloys by a multi-phase CALPHAD-coupled Kampmann-Wagner Numerical model. *Acta Materialia, 122*, 178-186. doi:https://doi.org/10.1016/j.actamat.2016.09.052

Furu, T., Marthinsen, K., & Nes, E. (1992). Paper presented at the Recrystallization*92, Fuentes and Sevillano, San Sebastian, Spain.

Humphreys, J., & Hatherly, M. (2004). *Recrystallization and Related Annealing Phenomena* (2. ed. ed.): Elsevier Ltd.

Jensen, L. E. (2013). *Varmetorsjonstesting av 3xxx legeringer [Hot torsion testing of 3xxx alloys]*. Retrieved from

Jensen, L. E. (2014). *Varmtorsjonstesting av 3xxx-legeringer [Hot torsion testing of 3xxx-alloys]*. (M.Sc.), Norwegian University of Science and Technology,

Jensrud, O. (2018). [Ad. basis materialet - 231465].

Kassner, M. E., & Barrabes, S. R. (2005). New developments in geometric dynamic recrystallization. *Materials Science and Engineering: A, 410-411*(Supplement C), 152-155. doi:https://doi.org/10.1016/j.msea.2005.08.052

Kassner, M. E., Myshlyaev, M. M., & McQueen, H. J. (1989). Large-strain torsional deformation in aluminum at elevated temperatures. *Materials Science and Engineering: A, 108*, 45-61. doi:https://doi.org/10.1016/0921-5093(89)90405-X

Kuhn, H., & Medlin, D. (2000). 10.3.1 Application to Metalworking Analyses. In *ASM Handbook, Volume 08 - Mechanical Testing and Evaluation*: ASM International.

Langeng, H. (2002). *Rekrystallisajon ved varmforming [Recrystallization by hot working]*. Retrieved from Unpublished:

Larsen, M. H. (2010). *Effect of composition and thermomechanical*
processing on the intergranular corrosion of
AA6000 aluminium alloys. (Philosophiae Doctor), Norwegian University of Science and Technology,

Lodgaard, L. (2000). *Precipitation of dispersoids containing Mn and/or Cr in Al-Mg-Si-alloys.* (PhD), The Norwegian University of Science and Technology,

Lohne, O., & Naess, O. J. (1980). The Effect of Dispersoids and Grain Size on Mechanical Properties of AlMgSi Alloys.

Loucif, A., Figueiredo, R. B., Baudin, T., Brisset, F., Chemam, R., & Langdon, T. G. (2012). Ultrafine grains and the Hall–Petch relationship in an Al–Mg–Si alloy processed by high-pressure torsion. *Materials Science and Engineering: A, 532*, 139-145. doi:https://doi.org/10.1016/j.msea.2011.10.074

Marioara, C. D., Andersen, S. J., Jansen, J., & Zandbergen, H. W. (2001). Atomic model for GP-zones in a 6082 Al–Mg–Si system. *Acta Materialia, 49*(2), 321-328. doi:https://doi.org/10.1016/S1359-6454(00)00302-5

Marioara, C. D., Andersen, S. J., Stene, T. N., Hasting, H., Walmsley, J., Van Helvoort, A. T. J., & Holmestad, R. (2007). The effect of Cu on precipitation in Al–Mg–Si alloys. *Philosophical Magazine, 87*(23), 3385-3413. doi:10.1080/14786430701287377

Matsuda, K., Ikeno, S., Uetani, Y., & Sato, T. (2001). Metastable phases in an Al-Mg-Si alloy containing copper. *Metallurgical and Materials Transactions A, 32*(6), 1293-1299. doi:10.1007/s11661-001-0219-2

McQueen, H. J., Knustad, O., Ryum, N., & Solberg, J. K. (1985). Microstructural evolution in Al deformed to strains of 60 at 400°C. *Scripta Metallurgica, 19*(1), 73-78. doi:https://doi.org/10.1016/0036-9748(85)90268-6

McQueen, H. J., & Ryan, N. D. (2002). Constitutive analysis in hot working. *Materials Science and Engineering A*.

Miller, W. S., Zhuang, L., Bottema, J., Wittebrood, A. J., De Smet, P., Haszler, A., & Vieregge, A. (2000). Recent development in aluminium alloys for the automotive industry. *Materials Science and Engineering: A, 280*(1), 37-49. doi:https://doi.org/10.1016/S0921-5093(99)00653-X

Mondolfo, L. F. (1976). *Aluminum Alloys: Structure and Properties*: Butterworth & Co Ltd.

Nadai, A. (1950). *Thory of Flow and Fracture of Solids* (2 ed. Vol. 1). New York: McGraw-Hill Book Company.

National Instruments. (2018). PID Algorithms. Retrieved from http://zone.ni.com/reference/en-XX/help/371361P-01/lvpidmain/pid_algs/

Park, H., & Lee, D. N. (2001). Deformation and annealing textures of drawn Al–Mg–Si alloy tubes. *Journal of Materials Processing Technology, 113*(1), 551-555. doi:https://doi.org/10.1016/S0924-0136(01)00658-6

Pettersen, T., Holmedal, B., & Nes, E. (2003). Microstructure development during hot deformation of aluminum to large strains. *Metallurgical and Materials Transactions A: Physical Metallurgy and Materials Science, 34*(12), 2737-2744.

Ponweiser, N., Lengauer, C. L., & Richter, K. W. (2011). Re-investigation of phase equilibria in the system Al–Cu and structural analysis of the high-temperature phase η1-Al1−δCu. *Intermetallics, 19*(11), 1737-1746. doi:https://doi.org/10.1016/j.intermet.2011.07.007

Quan, G.-z., Liu, K.-w., Zhou, J., & Chen, B. (2009). Dynamic softening behaviors of 7075 aluminum alloy. *Transactions of Nonferrous Metals Society of China, 19*, s537-s541. doi:https://doi.org/10.1016/S1003-6326(10)60104-5

Reiso, O. (2004). Extrusion of AlMgSi Alloys. *Materials forum, 28*.

Ren, W. W., Xu, C. G., Chen, X. L., & Qin, S. X. (2018). Microstructure and critical strain of dynamic recrystallization of 6082 aluminum alloy in thermal deformation. *IOP Conference Series: Materials Science and Engineering, 369*, 012022. doi:10.1088/1757-899X/369/1/012022

Rist, P. (2016). *The Influence of Transient Change in Strain rate on Subgrain Size During Deformation by Torsion of AA6063.* (M.Sc.), Norwegian University of Science and Technology,

Ryen, Ø., Holmedal, B., Marthinsen, K., & Furu, T. (2015). *Precipitation, strength and work hardening of age hardened aluminium alloys.* Paper presented at the IOP Conference Series: Materials Science and Engineering.

Rønning, B. (1998). *Constitutive relationships for AlZnMg, AlZnMgCr, and AlZrMgZr alloys.* (PhD), Norwegian University of Science and Technology,

Sandvik, J., Jensrud, O., Gulbrandsen-Dahl, S., Hallem, H., & Moe, J. I. (2010). Through Process Prevention of Recrystallization in Hot Formed Aluminium Structural Car Components *Materials Science Forum, 638-642*, 315-320

Sellars, C. M., & McTegart, W. J. (1966). On the mechanism of hot deformation. *Acta Metallurgica, 14*(9), 1136-1138. doi:https://doi.org/10.1016/0001-6160(66)90207-0

Shi, H., McLaren, J., Sellars, C. M., Shahani, R., & Bolingsbroke, R. (1997). Constitutive equations for high temperature flow stress of aluminium alloys. *Materials Science and Technology, 13*(3), 210-216. doi:10.1179/mst.1997.13.3.210

Smallman, R. E., & Ngan, A. H. W. (2014). *Modern Physical Metallurgy* Elsevier Ltd.

Valberg, H. S. (2010). *Applied Metal Forming Including FEM Analysis*: Cambridge University Press.

Vissers, R., van Huis, M. A., Jansen, J., Zandbergen, H. W., Marioara, C. D., & Andersen, S. J. (2007). The crystal structure of the β′ phase in Al–Mg–Si alloys. *Acta Materialia, 55*(11), 3815-3823. doi:https://doi.org/10.1016/j.actamat.2007.02.032

Wang, X., Guo, M., Chapuis, A., Luo, J., Zhang, J., & Zhuang, L. (2015). Effect of solution time on microstructure, texture and mechanical properties of Al–Mg–Si–Cu alloys. *Materials Science and Engineering: A, 644*, 137-151. doi:https://doi.org/10.1016/j.msea.2015.07.059

Wolverton, C. (2001). Crystal structure and stability of complex precipitate phases in Al–Cu–Mg–(Si) and Al–Zn–Mg alloys. *Acta Materialia, 49*(16), 3129-3142. doi:https://doi.org/10.1016/S1359-6454(01)00229-4

Xu, Y., Nagaumi, H., Han, Y., Zhang, G., & Zhai, T. (2016). The deformation behavior and microstructure evolution of a Mn- and Cr-containing Al-Mg-Si-Cu alloy during hot compression and subsequent heat treatment. *Metallurgical and Materials Transactions A*.

Yan, L.-Z., Zhang, Y.-A., Xiong, B.-Q., Li, X.-W., Li, Z.-H., Liu, H.-W., . . . Zhao, G. (2017). Mechanical properties, microstructure and surface quality of Al-1.2Mg-0.6Si-0.2Cu alloy after solution heat treatment. *Rare Metals, 36*(7), 550-555. doi:10.1007/s12598-015-0623-1

Zener, C., & Hollomon, J. H. (1944). Effect of Strain Rate Upon Plastic Flow of Steel. *Journal of Applied Physics, 15*(22). doi:10.1063/1.1707363

Zhao, Q., Holmedal, B., & Li, Y. (2013). Influence of dispersoids on microstructure evolution and work hardening of aluminium alloys during tension and cold rolling. *Philosophical Magazine, 93*(22), 2995-3011. doi:10.1080/14786435.2013.794315

Appendix A – Rotation speed, maximum moment and deformation temperature.

ω [rad/s]		$M_{T,\,max}$ [Nm]		$T_{Deformation}$ [°C]		$\dot{\gamma}$ [s^{-1}]		m
Average	**S.D.**	**Average**	**S.D.**	**Average**	**S.D.**	**Average**	**S.D**	
5,81	0,27	13,02	0,04	345,6	1,0	2,90	0,13	0,062
5,89	0,32	12,93	0,24	347,2	0,7	2,95	0,16	0,062
5,80	0,55	12,24	0,21	348,6	0,6	2,90	0,28	0,062
5,95	0,56	12,35	0,18	349,0	0,5	2,98	0,28	0,062
0,20	0,02	10,01	0,19	349,9	2,4	0,10	0,01	0,062
0,20	0,04	10,66	0,18	349,9	2,0	0,10	0,02	0,062
0,20	0,03	9,78	0,37	350,0	2,2	0,10	0,01	0,062
3,49	0,24	11,81	0,09	351,4	1,4	1,75	0,12	0,062
1,97	0,10	10,88	0,06	352,4	1,4	0,98	0,05	0,062
2,02	0,06	10,91	0,05	352,4	1,4	1,01	0,03	0,062
2,05	0,13	12,14	0,15	352,5	1,2	1,03	0,06	0,062
5,83	0,24	12,82	0,05	353,8	1,3	2,92	0,12	0,062
6,03	0,57	11,12	0,19	362,7	0,7	3,01	0,28	0,064
19,46*	1,32	10,58	0,23	379,0	1,2	9,73	0,66	0,067
5,37	0,18	8,42	0,10	394,3	1,2	2,68	0,09	0,070
5,76	0,26	8,77	0,34	394,7	1,0	2,88	0,13	0,070
6,21	0,41	7,69	0,20	398,3	0,5	3,11	0,21	0,071
2,06	0,12	8,26	0,15	398,9	4,4	1,03	0,06	0,071
3,48	0,18	8,34	0,05	399,3	1,3	1,74	0,09	0,071
0,20	0,03	6,38	0,32	399,8	2,0	0,10	0,01	0,071
0,21	0,03	6,82	0,15	400,2	2,2	0,10	0,01	0,071
26,53*	7,40	8,99	0,20	400,3	0,2	13,27	3,70	0,071
6,45	0,22	9,09	0,06	401,3	1,2	3,22	0,11	0,071
1,96	0,06	7,37	0,10	402,2	2,5	0,98	0,03	0,071
1,99	0,10	7,24	0,06	402,2	2,5	0,99	0,05	0,071
5,80	0,28	7,54	0,04	411,4	1,2	2,90	0,14	0,081
20,64*	0,97	7,89	0,18	424,3	1,0	10,32	0,49	0,094
2,04	0,11	5,32	0,07	447,9	1,9	1,02	0,06	0,118
5,79	0,19	6,50	0,04	448,0	0,3	2,90	0,10	0,118
5,86	0,44	5,72	0,04	448,6	1,1	2,93	0,22	0,118
5,85	0,22	6,04	0,09	448,9	0,8	2,92	0,11	0,118
0,20	0,03	4,20	0,10	449,4	1,8	0,10	0,01	0,118
0,20	0,03	4,03	0,10	450,1	1,5	0,10	0,01	0,118
6,24	0,24	6,32	0,05	452,0	0,2	3,12	0,12	0,118
3,43	0,13	5,59	0,03	453,0	1,1	1,71	0,06	0,118
2,01	0,08	4,16	0,06	498,6	1,5	1,00	0,04	0,118
6,92	0,50	5,08	0,06	499,0	2,8	3,46	0,25	0,118
0,20	0,02	3,33	0,11	499,3	2,2	0,10	0,01	0,118
6,10	0,43	4,95	0,04	501,3	0,5	3,05	0,22	0,118
5,83	0,18	4,35	0,06	512,0	0,1	2,92	0,09	0,117
2,05	0,09	3,31	0,05	545,8	0,7	1,03	0,05	0,115
5,79	0,77	3,91	0,07	547,7	0,5	2,89	0,39	0,115
0,21	0,02	2,66	0,11	549,3	1,6	0,10	0,01	0,115
6,27	0,29	3,94	0,09	550,6	0,1	3,13	0,15	0,115

*Without gear unit, i.e. the gear ratio was 1:1.

Appendix B – Strain rate and maximum stress

$T_{Deformation}$ [°C]		$\dot{\gamma}$ [s^{-1}]		$\dot{\varepsilon}$ [s^{-1}]		τ_{max} [MPa]		σ_{max} [MPa]		m
Avg.	**S.D**	**Avg.**	**S.D**	**Avg.**	**S.D**	**Avg.**	**S.D**	**Avg.**	**S.D**	
345.6	1.0	2.90	0.13	1.68	0.08	50.77	0.14	87.93	0.24	0.0617
347.2	0.7	2.95	0.16	1.70	0.09	50.40	0.94	87.29	1.63	0.0617
348.6	0.6	2.90	0.28	1.67	0.16	47.70	0.81	82.62	1.41	0.0617
349.0	0.5	2.98	0.28	1.72	0.16	48.14	0.72	83.38	1.24	0.0617
349.9	2.4	0.10	0.01	0.06	0.01	39.02	0.76	67.58	1.31	0.0617
349.9	2.0	0.10	0.02	0.06	0.01	41.55	0.70	71.96	1.22	0.0617
350.0	2.2	0.10	0.01	0.06	0.01	38.14	1.45	66.06	2.51	0.0617
351.4	1.4	1.75	0.12	1.01	0.07	46.04	0.36	79.75	0.63	0.0617
352.4	1.4	1.01	0.03	0.58	0.02	42.51	0.21	73.64	0.36	0.0617
352.4	1.4	0.98	0.05	0.57	0.03	42.41	0.23	73.45	0.40	0.0617
352.5	1.2	1.03	0.06	0.59	0.04	47.34	0.60	82.00	1.04	0.0617
353.8	1.3	2.92	0.12	1.68	0.07	49.98	0.20	86.57	0.35	0.0617
362.7	0.7	3.01	0.28	1.74	0.16	43.36	0.74	75.10	1.29	0.0636
379.0	1.2	9.73	0.66	5.62	0.38	41.33	0.89	71.59	1.53	0.0671
394.3	1.2	2.68	0.09	1.55	0.05	32.90	0.37	56.98	0.65	0.0703
394.7	1.0	2.88	0.13	1.66	0.07	34.28	1.33	59.38	2.31	0.0703
398.3	0.5	3.11	0.21	1.79	0.12	30.06	0.76	52.06	1.32	0.0713
398.9	4.4	1.03	0.06	0.60	0.03	32.31	0.58	55.96	1.01	0.0713
399.3	1.3	1.74	0.09	1.00	0.05	32.61	0.19	56.49	0.32	0.0713
399.8	2.0	0.10	0.01	0.06	0.01	24.94	1.24	43.20	2.15	0.0713
400.2	2.2	0.10	0.01	0.06	0.01	26.65	0.58	46.17	1.01	0.0713
400.3	0.2	13.27	3.70	7.66	2.14	35.15	0.77	60.88	1.33	0.0713
401.3	1.2	3.22	0.11	1.86	0.06	35.55	0.24	61.57	0.42	0.0713
402.2	2.5	0.98	0.03	0.57	0.02	28.82	0.41	49.92	0.70	0.0713
402.2	2.5	0.99	0.05	0.57	0.03	28.32	0.25	49.06	0.43	0.0713
411.4	1.2	2.90	0.14	1.67	0.08	29.57	0.17	51.22	0.30	0.0807
424.3	1.0	10.32	0.49	5.96	0.28	31.09	0.72	53.85	1.25	0.0936
447.9	1.9	1.02	0.06	0.59	0.03	21.13	0.29	36.59	0.50	0.1185
448.0	0.3	2.90	0.10	1.67	0.06	25.81	0.17	44.71	0.30	0.1185
448.6	1.1	2.93	0.22	1.69	0.13	22.69	0.17	39.31	0.29	0.1185
448.9	0.8	2.92	0.11	1.69	0.06	24.00	0.34	41.57	0.59	0.1185
449.4	1.8	0.10	0.01	0.06	0.01	16.68	0.40	28.89	0.69	0.1185
450.1	1.5	0.10	0.01	0.06	0.01	15.99	0.40	27.69	0.70	0.1185
452.0	0.2	3.12	0.12	1.80	0.07	25.08	0.20	43.44	0.35	0.1185
453.0	1.1	1.71	0.06	0.99	0.04	22.19	0.12	38.43	0.20	0.1184
498.6	1.5	1.00	0.04	0.58	0.02	16.53	0.22	28.63	0.38	0.1180
499.0	2.8	3.46	0.25	2.00	0.14	20.17	0.22	34.94	0.38	0.1180
499.3	2.2	0.10	0.01	0.06	0.01	13.23	0.43	22.91	0.74	0.1180
501.3	0.5	3.05	0.22	1.76	0.13	19.63	0.17	34.01	0.30	0.1180
512.0	0.1	2.92	0.09	1.68	0.05	17.25	0.22	29.88	0.38	0.1174
545.8	0.7	1.03	0.05	0.59	0.03	13.13	0.21	22.74	0.37	0.1153
547.7	0.5	2.89	0.39	1.67	0.22	15.51	0.28	26.87	0.49	0.1153
549.3	1.6	0.10	0.01	0.06	0.01	10.55	0.43	18.27	0.74	0.1153
550.6	0.1	3.13	0.15	1.81	0.08	15.64	0.35	27.08	0.61	0.1153

Appendix C – Zener-Hollomon values and microstructure categorization.

Z		$\ln(Z)$		$T_{Heat\ treated}$ [°C]	Micro-structure
Average	**S.D.**	**Average**	**S.D.**	**Average ± 2 °C**	
3,45E+11	2,23E+10	26,57	0,06	497	**Deformed fibrous grains**
3,45E+11	2,23E+10	26,57	0,06	539	
3,45E+11	2,23E+10	26,57	0,06	549	
1,69E+12	1,49E+11	28,15	0,09	418	
3,37E+12	3,59E+11	28,85	0,11	429	
3,37E+12	3,59E+11	28,85	0,11	478	
1,62E+13	1,99E+12	30,42	0,12	398	
1,62E+13	1,99E+12	30,42	0,12	447	
3,14E+13	3,67E+12	31,08	0,12	418	
3,14E+13	3,67E+12	31,08	0,12	459	
3,45E+11	2,23E+10	26,57	0,06	560	
1,58E+13	2,35E+12	30,39	0,15	490	
1,58E+13	2,35E+12	30,39	0,15	480	
1,58E+13	2,35E+12	30,39	0,15	470	
2,34E+14	5,16E+13	33,09	0,22	400	
2,34E+14	5,16E+13	33,09	0,22	355	
3,23E+13	1,93E+12	31,11	0,06	470	
1,69E+12	1,49E+11	28,15	0,09	539	**Mixed structure**
1,58E+13	2,35E+12	30,39	0,15	500	
1,68E+14	2,62E+13	32,75	0,16	398	
1,68E+14	2,62E+13	32,75	0,16	447	
1,68E+14	2,62E+13	32,75	0,16	478	
1,62E+14	3,58E+13	32,72	0,22	490	
3,24E+14	6,82E+13	33,41	0,21	520	**Recrystallized with small grains (D < 0.5mm)**
3,24E+14	7,19E+13	33,41	0,23	488	
3,54E+14	5,04E+13	33,50	0,14	498	
1,62E+14	3,58E+13	32,72	0,22	500	
3,24E+14	6,82E+13	33,41	0,21	470	
2,34E+14	5,16E+13	33,09	0,22	520	
1,68E+14	2,62E+13	32,75	0,16	518	
3,24E+14	7,19E+13	33,41	0,23	459	
3,24E+14	6,82E+13	33,41	0,21	450	

1,62E+14	3,58E+13	32,72	0,22	480	
1,62E+13	1,99E+12	30,42	0,12	549	**Recrystallized with medium sized grains (0.5 < D < 1.5 mm)**
3,24E+14	6,82E+13	33,41	0,21	430	
3,24E+14	7,19E+13	33,41	0,23	418	
1,69E+12	1,49E+11	28,15	0,09	539	
3,14E+13	3,67E+12	31,08	0,12	539	
3,46E+12	2,70E+11	28,87	0,08	550	
3,46E+12	2,70E+11	28,87	0,08	540	
3,37E+12	3,59E+11	28,85	0,11	549	**Recrystallized with large grains (D > 1.5mm)**
3,30E+13	4,44E+12	31,13	0,14	485	
3,30E+13	4,44E+12	31,13	0,14	465	
2,34E+14	5,16E+13	33,09	0,22	450	
3,46E+12	2,70E+11	28,87	0,08	530	
3,46E+12	2,70E+11	28,87	0,08	520	
3,24E+14	7,19E+13	33,41	0,23	398	
3,23E+13	1,93E+12	31,11	0,06	500	
3,54E+14	5,04E+13	33,50	0,14	520	
1,18E+14	1,67E+13	32,40	0,14	470	
3,14E+13	3,67E+12	31,08	0,12	497	
3,30E+13	4,44E+12	31,13	0,14	476	
3,23E+13	1,93E+12	31,11	0,06	490	
1,62E+13	1,99E+12	30,42	0,12	497	
3,23E+13	1,93E+12	31,11	0,06	480	
1,18E+14	1,67E+13	32,40	0,14	450	